POLITECNICO DI TORINO

Master Degree course in Nanotechnologies for ICTs

Master Degree Thesis

Structural characterization of tin halide perovskites for solar energy conversion

Supervisors
Prof. Andrea Lamberti
Dott.ssa Isabella Poli

Candidate
Giovanni Perinetti

Academic Year 2024-2025

Abstract

The growing global energy demand and the urgency of mitigating climate change have driven intense research toward sustainable materials for solar energy conversion. Among the various emerging semiconductors, metal halide perovskites (MHPs) with typical ABX_3 structure have recently gained attentions thanks to their remarkable optical tunability and low-cost fabrication routes, therefore emerging as promising materials for next generation optoelectronic and photocatalytic technologies. Within this class, tin-based perovskites (THPs) are considered the most viable alternative to toxic lead analogues. However, their widespread adoption remains limited by the intrinsic instability of the Sn^{2+} oxidation state, which rapidly converts into Sn^{4+} in the presence of oxygen , leading to structural and electronic degradation. One strategy to increase the structural stability of perovskites is tuning their composition, particularly the A-site cation. In this work, we study the use of dimethylammonium (DMA^+) as A-site cation to form DMASnBr3 and DMASnI3. These two compounds were prepared by planetary ball-milling, a green and scalable method that ensures high stoichiometric control, easy scalability and high reproducibility. Structural, optical, and thermal properties of the synthesized materials were analyzed using X-ray diffraction (XRD), UV-Vis spectroscopy, and thermogravimetric analysis (TGA). Particular attention was dedicated to assessing their stability under different atmospheric conditions, namely N_2, O_2, ambient air, and deionized water. Both compositions show exceptional structural stability toward O_2 but reduced stability towards moisture/liquid water. $DMASnI_3$ exhibited a distinct chromogenic transition, rapidly turning from yellow to black upon air exposure, associated with partial oxidation and amorphization, forming a hydrated phase. In the presence of liquid water $DMASnI_3$ transformed into SnI_4 but reversibly returned to the hydrated phase when the material was dried. In contrast, $DMASnBr_3$ demonstrated overall higher structural stability than $DMASnI_3$, moreover, the presence of moisture and liquid water generated a composite material where $DMASnBr_3$ coexisted with $(DMA)_2SnBr_6$ phase. Results highlight the critical influence of environmental agents on the degradation pathways of tin halide perovskites and provide valuable insight into the mechanisms governing their oxidation behavior, which is fundamental to fabricate efficient materials for solar energy conversion and photocatalytic applications.

Contents

List of Figures

List of Tables

Chapter 1

Introduction

1.1 The energy transition and solar technologies role

The global energy demand continues to grow at an accelerating pace. According to the International Energy Agency (IEA), the world's energy consumption grew by 2.2% in 2024, a notably faster rate than the average +1.3% observed over the previous 2013-2023 decade (figure 1.1a) [10]. Recent structural trends such as increased access to electricity intensive appliances, a net shift towards electric heavy manufacturing, upcoming power demands of digitalization, data centers, and the AI (artificial intelligence) industry, they all have driven and accelerated global electricity demand, which grew by +4.3% in 2024. Within this evolving landscape, renewables have become the dominant force in meeting the new growing demand (not only for electricity itself) accounting for the largest share (+38%) of the growth in total energy supply (Fig. 1.1b). On top of that, the last decade has seen a frightening increase global concern over climate change. In the framework of leading the world global transition towards a low-carbon economy, it is necessary to keep up with the rapid growth of energy demand through clean, efficient and sustainable technologies while (of course) avoiding fossil fuels [11]. Solar energy is playing a significant part due to its abundance and wide availability. Research studies in this field focuses on two complementary pathways: photovoltaics (PV) and photocatalysis (PC). Solar PV has been at the forefront of this transition, continuing its remarkable trend: global solar PV generation has approximately doubled every three years since 2016, a rate of expansion it maintained between 2021 and 2024 [10]. PV technology directly converts sunlight into electricity, feeding green power into the grid, meanwhile, PC uses solar energy to drive chemical reactions, such as producing hydrogen fuel from water (water hydrolisis) [12, 13]. While PV decarbonizes the electricity sector, solar fuels like hydrogen provide a significant energy vector to decarbonize sectors that are otherwise challenging to directly electrify, such as heavy transport and industrial processes [14]. The development of both technologies is therefore necessary (but not sufficient in my opinion) for a comprehensive replacement of fossil fuels and for mitigating the growing energy demand.

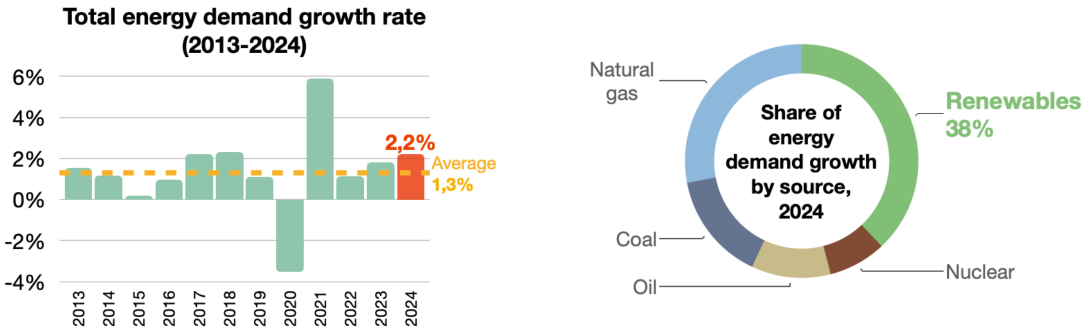

(a) (b)

Figure 1.1: **Panel (a)**: Global energy demand growth rate from 2013 to 2024. Reproduced from: IEA, World Energy Statistics and Balances, IEA, Paris `https://www.iea.org/data-and-statistics/data-product/world-energy-statistics-and-balances`. Licence: Terms of Use for Non-CC Material.
Panel (b): Pie chart of the share of energy demand growth by source in 2024. Reproduced from: IEA (2025), Share of energy demand growth by source, 2024, IEA, Paris `https://www.iea.org/data-and-statistics/charts/share-of-energy-demand-growth-by-source-2024`, Licence: CC BY 4.0

1.2 Semiconductors: the heart of photoconversion processes

The working principle of both PV and PC device systems is based on semiconductors. These materials are the backbone of the modern technological era, underpinning the entire electronics industry from microprocessors and memory chips to sensors and displays. Their unparalleled versatility stems from the ability to precisely engineer their optical and electronic properties through doping, compositional tuning, and nanostructuring [15]. This technique of tailoring optoelectronic properties is what makes semiconductors equally indispensable for energy applications too, where they can be designed to efficiently convert light into electric charges. The optoelectronic properties of a semiconductor are mainly defined by its electronic band structure. Particular attention is given to the energy band-gap (E_g) which determines the portion of light spectrum that the material can absorb and, consequently, the maximum theoretical efficiency for converting photons into useful energy [16]. Altough E_g value is fundamental, even more important is the type of band gap that the semiconductor intrinsicaly exhibits. When the minimum point of conduction band (CB) and the maximum point of valence band (VB) are alligned in the reciporocal space $\vec{k}$, the band gap is direct, otherwise it is indirect (Fig. 1.2). Light absorption mechanism is different between direct and indirect gaps. When a direct band gap semiconductor interacts with a photon having energy greater than its bandgap ($E_{ph} \geq E_g$), an electron is promoted from VB to CB, generating an electron-hole pair (our electric charge). On the other hand, for an indirect band gap type, the photogenration process involves a third component other than electron and photon: a phonon. The reason of this third body to take part in the process is due to energy and momentum conservation that must be always be satisfied, and, because three-body interactions are less likely than two-body interactions, indirect band gap semiconductors are less efficient in absorbing and converting photons into electrical carriers. Regardless of the band gap type, once the *e*-*h* pairs are generated they can be collected as an electrical current (photovltaic applications), or they can be directly exploited to drive specific chemical reactions, such as oxydation ot reduction of targer species (photocatalysis applications) [17]. Appropriate energy band gap value depend on the specific application: in general photovoltaic ask for energy band gaps between 1 eV and 1.5 eV, mostly due to the solar spectrum irradiance, whereas for photocatalysis it mainly depends on the target chemical reaction and more importantly the absolute postions of CB and VB must be aligned with the correspective reduction/oxydation target potentials. Charge transport is aslo crucial: high mobility and long diffusion lenght are necessary to ensure sufficiently long carrier lifetimes and to minimize their recombination before being collected [18]. Stability of the compound in acqueos solutions or specific pH ranges has to be assested before photocatalysis [19].

1.2.1 Established and emerging technologies: the path to perovskites

Historically, silicon has dominated the photovoltaic market due to its abundance, stability and efficiencies over 26% [20]. Silicon has an energy band gap of $E_g \simeq$ 1.12eV that quite alligns with PV requirement (1eV $< E_g <$ 1.5eV), however its band gap is of indirect type, which as described above, hinders the photoelectron generation. In order to achieve such high efficieny then, silicon devices for solar epplications require thick, highly pure and rigid wafers, making its production expensive and energy intensive, with manifacturing of monocrystalline silicon is mostly localized in Asia. Because of that, research has recently moved towards alternative semiconductors, organic and inorganic, with superior optical properties that would enable the production of more flexible, cheaper and potentially thin-film manufacturable devices [21]. This evolution led to the so-called "third-generation"

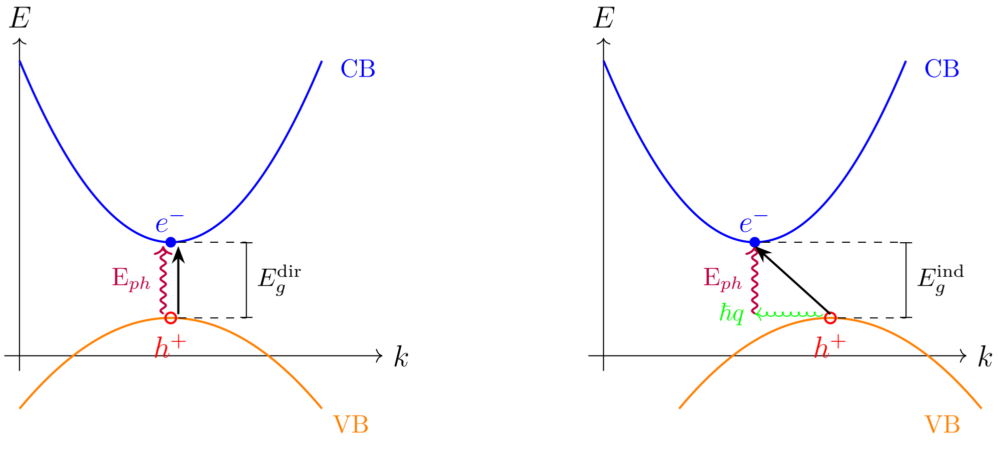

(a) (b)

Figure 1.2: Simplified representation of **(a)** direct and **(b)** indirect band gap in 1D reciprocal space k. E_{ph} is the photon energy impinging on the semiconductor, $\hbar q$ is the phonon energy, e^- and h^+ are the electron and hole respectively.

or *emerging photovoltaics*, which include: dye-sensitized solar cells (DSSCs), organic photovoltaics (OPV), and, more recently, perovskite solar cells (PSCs) [22]. In this work we are going to focus on the materials that characterizes the latter technology: perovskites.

1.3 Perovskite and perovskites

The term *perovskite* originally comes from russian mineralogist Lev Perovskij and it refeers firstly to calcium titante mineral $CaTiO_3$ [23]. Nowadays perovskite materials (or structures) apply instead to all those compounds that share the same ABX_3 chemical formula and crystallize in a three-dimensional framework composed of corner-sharing BX_6 octahedra, with the A cation occupying the interstitial sites [24]. A visualizzation of such description is shown in figure 1.3. Despite the

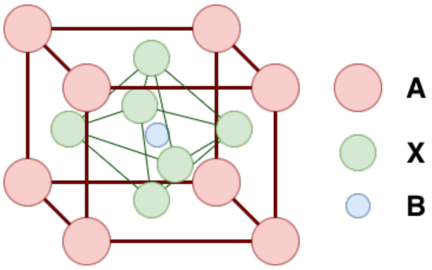

Figure 1.3: Ideal cubic crystal structure of a perovskite with formula ABX_3.

ideal and simple cubic arrangement mentioned above, there exist an enormous and vast variety of strucutrual arrangement within this class of material. Distorsions in the unit cell are very common and they are entirely controlled by the geometry of cation/anion combinations. The versatility and wide spectrum properties are in fact not only due to chemical nature of perovskite elements, but also direct consequences of how they accomodate within the unit cell. A common way to predict which crystal structure a particular combination of ions in an ABX_3 perovskite will form is to calculate the empirical tolerance factor t (Equation 1.1). This simple but powerful geometric parameter is calculated from the ionic radii:

$$t = \frac{r_A + r_X}{\sqrt{2}\,(r_B + r_X)} \tag{1.1}$$

where r_A, r_B and r_X are the ionic radii of the A, B and X sites, respectively. According to the literature, stable (but not cubic) 3D perovskite phases typically occur for $0.8 < t < 1$. Ideal cubic unit cell is achieved when $t = 1$ [25]. Deviations from this range can induce distortions into tetragonal, orthorhombic, or rhombohedral phases which can be potentially less stable.

Even tough in this work we're going to appreciate and discuss a rather small bit of the physical and chemical properties of perovkites as photosensitive semiconductors, it is truly important to highlight and remark the high versatilty of these materials. There exist hundreds (if not thousand) of chemical combinations and each one of them can be tuned to obtain specific unique properties such as: ferroelectricity, antiferromagneticity, piezoelectricity, or even act as insulators, conductors and in some cases superconductors. This extreme tunability has allowed researcher in the optoelectronic framework to develop not only applications in photovoltaic and photo-catalysis, but even light emission and energy storage applications [26, 27].

1.3.1 Metal halide perovskites and their optoelectronic applications

There exist several subclass of perovskites. In this work we're going to focus our attention on the so called *metal halide perovskites* (MHPs), which occur when the A site is occupied by an organic or inorganic monovalent cation (e.g., Cs^+, $MA^+ = CH_3NH_3^+$), the B site is a divalent metal cation such as Pb^{2+} or Sn^{2+}, and the X site is a halide anion (Cl^-, Br^-, I^-). The most common and widely studied halides are iodide (I^-) and bromide (Br^-). MHPs are semiconductors with direct band gaps, whose optoelectronic properties can be finely tuned by changing the A, B, or X components. The valence and conduction band edges of MHPs are primarily defined by the interaction between orbitals of the B-site metal cation and the X-site halide anions. Consequently, changing the identity (or mixing) of X site significantly affects the band structure, allowing for fine-tuning of the bandgap: it has been observed that bromide compositions typically yield to wider bandgaps, while iodide compositions result in narrower bandgaps [26, 28]. This versatility has led to their extensive exploration in solar cells, light-emitting devices, lasers, and photodetectors.

1.3.2 Perovskites Solar Cells: opportunities and challenges

In the context of solar applications, perovskite solar cells (PSCs) have rapidly emerged as one of the most promising technologies since their efficiency increased from 3.8 % in 2009 to over 26 % in 2024, nearly closing the efficiency gap with silicon (Figure 1.4) [1].

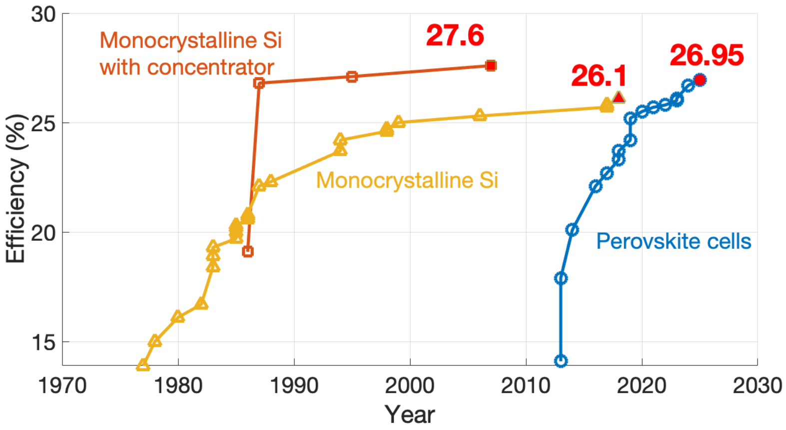

Figure 1.4: Efficiency chart of the most efficient solar cell types from 1990 to 2025. A concentrator is a type of PV system that exploits curved mirrors or lenses to concentrate light in a confined spot. Data is reproduced from *NREL,Best Research-Cell Efficiency Chart* [1].

This achievement is due their outstanding and versatile optoelectronic properties, specifically they satisfy all the key requirements that an efficient PV device should have:

- High absorption coefficient, so a very thin layer (around 500 nm) is enough to absorb light. This allows for the fabrication of thin, lightweight solar cells [29].
- A direct and tunable bandgap. By changing the composition (e.g., mixing iodine and bromide), the bandgap can be adjusted from 1.2 eV to 3 eV, enabling the optimization of the material for different parts of the solar spectrum or for tandem applications [28]
- Long carriers diffusion lengths (> 1 µm), so that charges can travel far within the material and be efficiently collected before recombining [30]

- They can be made from liquid solutions at low temperatures, which is a cheap processing method compatible with flexible substrates and roll-to-roll manufacturing unlike traditional high-temperature silicon processes [31, 32].

The most studied compound in this family is indeed methylammonium lead iodide ($MAPbI_3$), which has been widely investigated for perovskite solar cells and related optoelectronic applications, exhibiting outstanding photovoltaic performance, with power conversion efficiencies up to 22% [33]. However, $MAPbI_3$ suffers from two major drawbacks that represent huge challenges for commercialization:

1. **Stability:** Quick degradation occurs when exposed to moisture, oxygen, or heat. This is a major problem for making commercial devices that need to last for many years [34].
2. **Lead:** The presence of lead poses environmental and safety risks, raising concerns for large-scale production and disposal [35].

Strategies to overcome these issues are focused on compositional engineering, dimensional control, and the development of sustainable synthesis routes.

Compositional engineering has been proven highly effective. Replacing the volatile methylammonium (MA^+) cation with a mixture of formamidinium (FA^+=$CH(NH)_2^+$) and cesium (Cs^+) has yielded the trivalent cation CsFAMA, which demonstrates significantly improved thermal and photo-stability while maintaining power conversion efficiencies (PCEs) above 20% [36].

Concurrently, research into lead-free alternatives intensified too. While tin (Sn^{2+}) is the most direct substitute thanks to similarity in both electronic structure and ionic radius can yield PCEs over 14% [37], its susceptibility to oxidation remains a challenge. This has spurred interest in searching new solution far from the classic ABX_3 structures, such as implementing a double perovskites ($A_2BB'X_6$) architecture, extending its versatility by hosting two different cations (mono or tri-valent) in the B site. This substitution not only allows fine-tuning of the band structure and defect chemistry, but also enables the design of materials with reduced toxicity. A relevant example is the family of lead-free halide double perovskites, such as $Cs_2AgBiBr_6$, which offers enhanced stability albeit with currently lower efficiencies ($\sim$6%) due to its indirect bandgap [38, 39].

Other options include exploring antimony (Sb^{3+}) and bismuth (Bi^{3+}) cations based perovskites like $Cs_3Sb_2I_9$ and $MA_3Bi_2I_9$, which trade-off efficiency for greatly improved environmental stability [40]. Another structure to be mentioned is the so called *vacancy ordered perovskite* with chemical formula A_2BX_6. It can be seen as a derivition from the $A_2BB'X_6$ structure where the B' cation is substituted with a vacancy (here it lies the *vacancy ordered* name) and the B cation is a tetravalent transition metal instead. A visual representation of these different structural types is shown in figure 1.5.

Beyond compositional engineering, dimensional control is a viable and powerful strategy. Starting from the 3D ABX_3, it is possible to achieve lower dimensional structures by strategically slicing the 3D framework using bulky organic cations [41]. This dimensional reduction is achieved by replacing the small A-site cation with a large, often ammonium-based, organic cation that cannot be accommodated within the confines of the BX_6 octahedral network. This bulky cation acts as a spacer, effectively cleaving the 3D structure into discrete slices, such as two-dimensional (2D) layers, one-dimensional (1D) chains, or zero-dimensional (0D) octahedra, which are separated by these organic insulating sheets. For example, by incorporating bulky organic cations, such as phenylethylammonium (PEA^+), it is possible to create layered 2D perovskites at the surface of 3D grains. These structures act as natural protective barriers, dramatically enhancing moisture resistance. For 2D perovskites specifically, this results in layered structures with the general formula $L_2A_{n-1}B_nX_{3n+1}$, where L represents the large organic cation and n defines the thickness of the inorganic slab (the number of octahedral layers). Solar cells employing these architectures have demonstrated operational stability for thousands of hours under accelerated aging tests, a critical milestone towards commercialization, morevoer this approach allows for precise tuning of the material's optoelectronic properties by controlling the dimensionality and the 'n' value, offering a powerful strategy for creating stable and tailored functional materials [42,43].

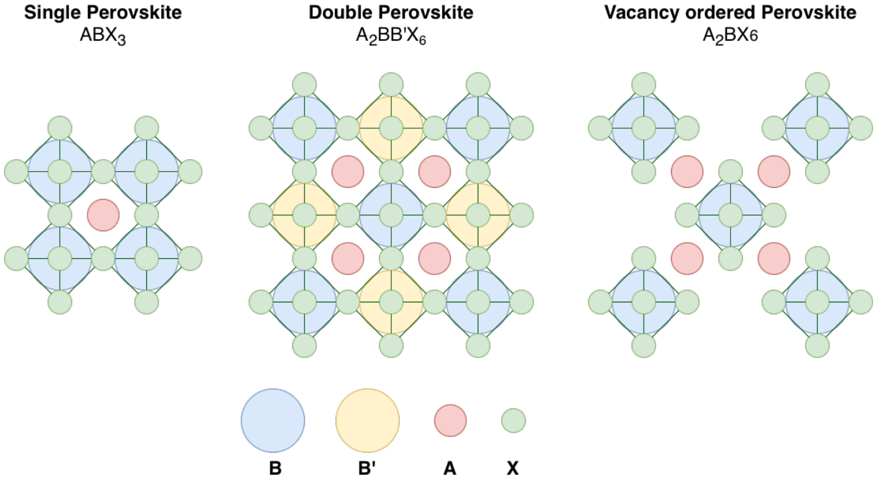

Figure 1.5: Double perovskite ($A_2BB'X_6$) structure and (A_2BX_6) vacancy ordered double perovskite structure.

1.3.3 Tin halide perovskites as lead-free alternative

Among lead-free alternatives, tin halide perovskites (THPs) represent one of the most promising directions due to their similar electronic configuration and ionic radius to lead-based counterparts. Compounds like $MASnI_3$ and $FASnI_3$ have reached efficiencies over 6-9% [44, 45]. However, the poor photovoltaic performance compared to lead-based perovskites and the tendency of Sn^{2+} to oxidize into Sn^{4+} have limited their widespread adoption [46].

Beyond the B cation, the A cation also plays a crucial role in structural and environmental stability. While methylammonium is a quite common choice for cation A site in literature, dimethylammonium cation ($DMA^+ = (CH_3)_2NH_2^+$) has been reported to improve resistance against moisture and atmospheric agents when exploited in tin-based perovskites [47]. This makes DMA-based THPs promising candidates for applications requiring stability under realistic environmental conditions.

Tin oxidation and instability issues

One of the most critical point that hinder THP large scale use is the chemical instability of Sn^{2+} cation, which occupies the B site in the perovskite structure (ABX_3), which readily oxidizes to Sn^{4+}. Even though tin and lead share a similar valence electron configuration, their chemical behaviour differs significantly due to relativistic effects on the outer electrons. This explains why tin halide perovskites are generally less stable than their lead-based counterparts. In particular, the 5s orbital of tin experiences weaker relativistic stabilization compared to the 6s orbital of lead, resulting in a lower binding energy and, consequently, reduced chemical inertia. This oxidation induces undesired p-type self-doping, increasing charge-carrier recombination rates and shortening carrier diffusion lengths [46, 48]. Such effects would be detrimental for the applications targeted in this work.

Despite that, there are several recent studies that have classified two novel THP with structure $DMASnX_3$ (X= Br, I) as stable and suitable PC applications, respectively: dimethylammonium tin bromide ($DMASnBr_3$) and dimethylammonium tin iodide ($DMASnI_3$) [4, 47, 49–52].

Typically, these THPs are characterized either directly after synthesis, which generally relies on solvent-based processes performed under ambient atmosphere, where dissolved oxygen or moisture can interfere with reactions thus inevitably leading to oxidation. To overcome these limitations, ball-milling synthesis could enable solvent-free processing and minimizes air exposure during preparation. Combined with glove-box handling for loading and extraction, this approach yields pristine powders suitable for reliable and controlled characterization. Furthermore, the measurements can be carried out under strictly defined atmospheric conditions, ranging from oxygen-rich to fully ambient environments. This controlled methodology provides a consistent baseline to assess how different environmental agents affect the stability of materials. It is clear that understanding the role of oxygen and moisture in the degradation pathways of the materials is crucial. For this reason, in this work we systematically investigated the stability of $DMASnBr_3$ and $DMASnI_3$ powders under different environments: N_2, O_2, air, and water.

1.3.4 $DMASnBr_3$ and $DMASnI_3$: reported stability and applications

Representative unit-cell pictures of $DMASnBr_3$ (Fig. 1.6a) and $DMASnI_3$ (Fig. 1.6b) taken from the available data in literature [2, 3]. These figures are meant to give a qualitative idea of the expected crystal geometry and the relative position of A, B and X atoms in the lattice.

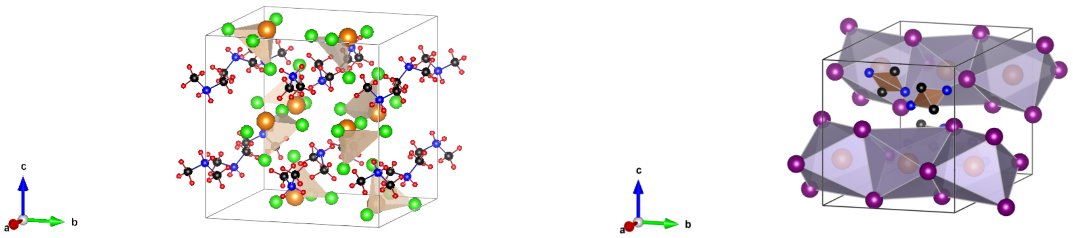

(a)

(b)

Figure 1.6: **Panel (a)**: Crystal structure of $DMASnBr_3$ reproduced with VESTA from CCDC-1315585 [2]. **Panel (b):** Crystal structure of $DMASnI_3$ reproduced with VESTA from CCDC-1854322 [3].
Legend: Red= H, Black= C, Blue= N, Green= Br, Purple= I, Orange= Sn.

Calculated values for the tin halides considered in this study are reported in Table 1.1.

Table 1.1: Goldschmidt tolerance factor *t* (from eq. 1.1) for $DMASnBr_3$ and $DMASnI_3$. Ionic radii are taken from Shannon et al. [8], with additional estimate value of DMA^+ cation from the literature [9].

	$\mathbf{r}_{DMA^+}$(Å)	$\mathbf{r}_{Sn^{2+}}$(Å)	$\mathbf{r}_{Br^-}$(Å)	$\mathbf{r}_{I^-}$(Å)	**t**
$DMASnBr_3$	2.72	1.18	1.96		1.05
$DMASnI_3$	2.72	1.18		2.20	1.03

Despite the remarked chemical instabilities of tin, $DMASnBr_3$ and $DMASnI_3$ perovskites show marked water stability when compared to conventional lead-based analogues and offer promising photo catalytic and optoelectronic performance. Romani et al. [49] reported that mechanochemical synthesized $DMASnBr_3$ composite with graphite carbon nitride ($g\text{-}C_3N_4$) withstands aqueous conditions-as confirmed by diffraction, optical, and X-ray photo-electron analyses, yielding hydrogen evolution rates greater than 1700 μmol g^{-1} h^{-1}. In studies of $DMASnI_3$, Tanaka et al. [50] described the formation of protective surface layers in polar solvents that alter both charge carrier dynamics and photo-luminescence in water containing dissolved oxygen, while Ju et al. [51] observed no decomposition after 16 h in de-ionized water and noted reversible band gap narrowing. DFT (density functional theory) investigation by Ju et al. [52] attributes improved water stability in $DMASnI_xBr_{3-x}$ materials to increased water adsorption energy, elevated osmotic barriers, and reduced intralayer spacing. Applications reported in these studies include photo-catalytic hydrogen evolution and NADH (nicotinamide adenine dinucleotide hydrogen) regeneration. Another study successfully exploited oxygen doped $DMASnI_3$ (namely $DMASnI_3(O)$) for CO_2 reduction and production of ethylene [4]. Optoelectronic measurements further suggest potential relevance for solar cell components, although direct evidence for sensor applications has not been provided.

Despite these encouraging results, limited data address the stability of $DMASnBr_3$ and $DMASnI_3$ in air, oxygen, or moisture beyond the noted effects on photoluminescence. This motivates a systematic study of their environmental degradation pathways, which is the focus of the present work.

1.3.5 Synthesis methods: from solution based method to mechanochemistry

Parallel to material design, an essential aspect is the development of sustainable and scalable synthesis methods that can go beyond traditional solution-based. Within this perspective, the push toward green synthesis and the exploration of novel compositions align with broader goals of sustainable energy and chemical production, such as the development of carbon-neutral technologies. Solution-based methods have been mostly used for their effectiveness in synthesizing metal halide perovskites with excellent crystalline quality [53, 54]. Typically, this type of process consists of dissolving precursors associated with MHP in a polar aprotic solvent, usually either DMSO (dimethyl sulfoxide) or DMF (dimethylformamide). Subsequently, thermal energy can be applied to promote crystallization and form the desired perovskite. When dealing with THP, it is necessary to add a strong reducing agent (e.g., hypophosphorous acid, H_3PO_2) to the precursor solution to prevent oxidation of the tin precursor. This approach is exploited for powder, crystal, and thin-film synthesis. Both DMSO and DMF have gained popularity for their effectiveness in solubilizing tin-based perovskites and their precursors, but there are many concerns associated with their high toxicity and poor sustainability [55]. For these reasons, it is necessary to either find new solvents that offer the same performance with a lower environmental impact and reduced safety hazards regarding handling in research and production lines, or to implement new synthesis methods that avoid solvents altogether. In this work, we focus on the latter approach, namely mechanochemistry. This technique has been successfully applied to synthesize a wide range of perovskites, from $MAPbI_3$ to lead-free variants like $Cs_2AgBiBr_6$ and even layered 2D phases, often yielding materials with comparable or even superior optoelectronic properties to their solution-processed counterparts [56, 57]. Mechanochemistry is a branch of chemistry in which chemical reactions are induced by mechanical force, typically through grinding or milling. This approach uses mechanical energy to activate or promote chemical transformations, often without or with minimal use of solvents. Mechanochemical reactions can be performed using various devices such as mortar and pestle, vibrational ball mills (VBM), planetary ball mills (PBM), shaker mills, tumbler ball mills, single-screw devices (SSD), and twin-screw extruders (TSE) for continuous flow processes. This technique aligns with green chemistry principles by significantly reducing the environmental footprint of chemical synthesis, since most mechanochemical reactions occur solvent-free or with minimal solvents, thereby avoiding the use of large volumes of harmful and toxic solvents common in traditional solution-based synthesis, which contributes to large amounts of hazardous waste and pollution. Moreover, even though mechanical energy is required, the overall energy consumption can be lower than that of heating or long reaction times in solution. Additionally, mechanochemical processes can avoid the need for cooling/heating cycles and hazardous reagents, therefore offering a viable path for industrial scale-up [58–60].

1.4 Research objectives

In this thesis, we point our focus on the mechanochemical synthesis and characterization for applications in photo-catalysis or photovoltaic of two tin halide perovskites: $DMASnBr_3$ and $DMASnI_3$. Bromide THP has already been synthesized through ball-milling, also proving its water stability [47, 49]. On the other hand, the iodide counterpart has not been mechanochemically synthesized yet, but there are scientific researches claiming the material's stability and a reversible phase behavior over air and water exposure [50–52]. Given this state of the art, we are setting the following objectives:

1. To investigate whether $DMASnBr_3$ and $DMASnI_3$ can be reliably synthesized by mechanochemical methods (ball milling).
2. To evaluate the reproducibility and stability of the obtained phases under ambient conditions and in contact with water.
3. To assess whether these materials can be considered promising candidates for solar energy conversion.

Chapter 2

Materials and methodology

2.1 Synthesis

Synthesis was carried out using a planetary/bench-top ball mill (Fritsch Pulverisette 7, figure 2.1) at 400 rpm for 40 minutes with a BPR (ball to powder ratio) of 1:10.

Figure 2.1: Fritsch Pulverisette 7 planetary ball-mill.

Table 2.1: Jar characteristics

Volume	**Material**
45 mL	Si_3N_4

Table 2.2: Balls characteristics

Size	**Material**	**Mass**
ϕ 10 mm	Si_3N_4	2.0048 g/ball

The stoichiometric of the involved reaction for the synthesis are the following:

$$\mathrm{DMAI} + \mathrm{SnI_2} \longrightarrow \mathrm{DMASnI_3}, \tag{2.1}$$

$$\mathrm{DMABr} + \mathrm{SnBr_2} \longrightarrow \mathrm{DMASnBr_3}. \tag{2.2}$$

During the 40 minutes milling, aliquots of mass ∼200 mg have been withdrawn every 10 minutes (therefore at 10, 20, 30 and 40 minutes respectively) for reaction monitoring purposes. Precursor loading and extraction of samples and final product has been carried out inside the glovebox, hence in inert Ar atmosphere. All the employed precursors were purchased from Sigma-Aldrich: DMAI (CAS n. 51066-74-1), SnI_2 (CAS n. 10294-70-9), DMABr (CAS n. 6912-12-5), $SnBr_2$ (CAS n. 10031-24-0). All compounds were stored and handled in glovebox straight after the purchasing due to their hygroscopic and air-sensitive nature.

In order to quantify precursor masses, molar fraction w was calculated as follows: Given a reaction like

$$aX + bY \longrightarrow cZ$$

where X and Y are the reactants, Z is the product while a, b, c are the corrispective involved moles. Then:

$$w_X = \frac{a}{c} \cdot \frac{MM_{\ X}}{MM_{\ Z}}$$

$$w_Y = \frac{b}{c} \cdot \frac{MM_{\ Y}}{MM_{\ Z}}$$

with MM being the molar mass. Then, by setting the amount of desired product ($m_Z|_{\text{desired}}$) to synthetize, computing the reactantant masses is straighforward as:

$$m_X = w_X \cdot m_Z|_{\text{desired}}$$

$$m_Y = w_Y \cdot m_Z|_{\text{desired}}$$

In table 2.3 are reported the molar fraction regarding the perovskites under study.

Table 2.3: Reactants molar masses (MM) and molar fractions related to reactions 2.1 and 2.2.

Reactants	DMABr	$SnBr_2$	DMAI	SnI_2
MM (g/mol)	126	278.52	173	372.52
Molar fraction	0.311	0.689	0.317	0.683

2.1.1 Samples preparation

When specified, for handling and optical measurements, the synthesized powders were pressed into pellets using an evacuable 10 mm die (figure 2.2b) paired with a pressing tool that can apply an equivalent applied load of 10 tons (figure 2.2a). Each powder is loaded into the die inside the glovebox and transferred to the pressing tool which is located outside the glovebox. The pressed powder is then removed from the die (now in form of pellet disks) and kept stored in glass vials inside the glovebox. It is important to note that a brief exposure to ambient air during the transfer to/from the pressing tool is unavoidable.

(a) (b)

Figure 2.2: **Panel (a):** pressing tool. **Pane (b):** evacuable 10 mm pellet die.

2.1.2 Thin films

Thin films of $DMASnI_3$ were fabricated via spin coating onto glass substrates of 2.5 cm × 2.5 cm pre-cleaned with acetone, isopropanol and a subsequent ozone treatment. The choice of glass as a substrate was motivated by its optical transparency, chemical stability, and wide use as a standard support for preliminary perovskite film investigations. The solvent selected for the deposition was 1-butanol (Sigma-Aldrich, ≥99%, CAS n. 71-36-3). Precursor solution was prepared by dissolving 100 mg of $DMASnI_3$ powder in 1 mL of 1-butanol, corresponding to a concentration of 100 mg/mL (100 g/L). This concentration was chosen as a reasonable compromise between achieving sufficient solubility for film formation and avoiding excessively concentrated dispersions that could hinder uniform deposition. The prepared solution was finely mixed with the help of a mini vortex) before deposition to minimize the presence of aggregates or undissolved particles. The deposited solution was then spin coated for 40s at 800rpm followed by a quenching at 120°C for 3 minutes.

2.2 Characterization techniques

Characterization is a fundamental step in understanding the properties and behavior of a material. It involves using a set of analytical techniques to probe its composition, structure, morphology, and functional response. Through these analyses, we can establish correlations between the synthesis conditions, the resulting structure, and the material's overall performance.

2.2.1 X-ray diffraction (XRD)

X-ray diffraction has been used for identifying the crystalline phase by measuring the angles and intensities of X-rays that undergo constructive interference on the lattice according to Bragg's law:

$$n\lambda = 2d\sin\theta \tag{2.3}$$

Each compound gives a unique diffraction pattern, much like of a personal fingerprint, therefore it is possible to classify and then recognize any material or compound through this technique. Three experimental setups have been used:

- **@DISAT, Turin**: PANanalytical X'Pert Pro-diffractometer .

  X-ray anode source: Cu Kα_1

  Voltage/current: 40 kV / 40 mA.

  Geometry: Bragg-Brentano parafocusing configuration.

  Operative temperature: room temperature (∼30°C).

- **@IIT-CCT, Genoa**: Third generation Empyrean diffractometer (Malvern PANalytical, Westborough, MA)

  1.8 kW Cu Kα X-ray

  Voltage/Current: 45 kV and 40 mA

  Automated prefix iCore-dCore optical modules, PIXcel3D area detector and Anton Paar TTK 600, a non-ambient chamber for X-ray diffraction studies from -190 °C to 600°C and in-situ measurements.

  XRD patterns from $2\theta = 5$ to $70°$ were collected in Bragg Brentano (BB) geometry with step size $2\theta = 0.026°$

  Each pattern acquisition required approximately 15 minutes. The analysis was carried out putting the samples on a zero-diffraction silicon substrate in air as well as under nitrogen and oxygen flow

  Data analysis was performed using the software HighScore Plus 5.3.1.

- **@ IIT-CNST, Milan**: Bruker D8 Advance

  Cu Kα1 ($\lambda = 1.544\,060\,\text{Å}$) anode source

  Voltage/Current: 40 kV and 40 mA.

  Glazing incidience (ω=2°)

  Diffraction patterns were collected at room temperature, with a step size of 0.05 in symmetric scan reflection mode and an acquisition time of 2 s.

2.2.2 Ultraviolet-visible spectroscopy (UV-Vis)

Ultraviolet–visible (UV–Vis) spectroscopy is a widely used analytical technique for investigating the optical properties of materials. A UV–Vis spectrometer measures how much light a sample absorbs or transmits in the ultraviolet and visible regions of the electromagnetic spectrum, typically between 200 and 900 nm. Typically each instrument is equipped with a lamp that emits in wide wavelenght range. The latter is then diffracted on a grating. Finally, the monochromatic light is shined through a sample and the transmitted/absorbed intensity is compared with that of a reference. From this comparison, the absorbance spectrum is obtained. Band gaps were estimated by measuring the diffuse reflectance spectra of the samples with a Perkin-Elmer Lambda 650 spectrophotometer equipped with a 150 mm integrating sphere @IIT-CSFT, Turin. Because suspending the powders in a solvent could induce decomposition (especially for the iodide compound), spectra were acquired on the pressed pellets in diffuse reflectance mode. Details regarding pellets preparation is contained in the relative section. Note: the exploited set-up does not allow in-situ inert atmosphere; samples were therefore exposed to ambient air during optical measurements. Potential oxydation during acquisition is discussed where relevant.

2.2.3 Scanning electron microscope (SEM)

Field Emission Scanning Electron Microscopy (FESEM) for sample's morphological analysis has been performed with a Zeiss FESEM Supra40 @DISAT,Turin, equipped with InLens and secondary electrons detector. Top-view images were collected operating at 5kV with an aperture size of 30 mm. Working distance and relative magnification are instead specified each time a picture is displayed. Powder samples were prepared depending on the target atmopsheric agent as follows:

- **Pristine:** inside an argon filled glovebox, the powder was disperded on a carbon-taped sample holder and stored inside a glass vial untill the loading in FESEM chamber.
- **Oxygen exposed:** inside an argon filled glovebox, the powder was disperded on a carbon-taped sample holder and stored inside a glass vial. Then the

same glass vial was saturated with pure oxygen and closed right after untill the loading in FESEM chamber.

- **Air exposed:** the powder was disperded on a carbon-taped sample holder and stored inside a glass vial in normal atmospheric condition untill the loading in FESEM chamber.
- **Water exposed:** the powder was firstly wetted with DIW, let it dried under a fumehood and then disperded on a carbon-taped sample holder and stored inside a glass vial untill the loading in FESEM chamber.

2.2.4 Thermogravimetric analysis (TGA)

TGA was employed to determine thermal stability and decomposition temperatures of the synthesized powders. This technique records the mass change of a material as it is heated, providing a direct measure of thermal stability, decomposition pathways, and residue formation. Thermogravimetric analysis was carried out with a Netzsch TG 209 F1 Libra coupled with a Bruker Tensor II spectrometer, a standardized 165mg Al_2O_3 crucible and 20°C/min heat ramp. When specified a 20mL/min N_2 flow is purged on the crucible. Three main signals have been recorded during each measurment as function of temperature:

- Realtive mass loss (TG). Direct and main measure of the TGA, it gives us in percentual how much mass the sample loses from room temperature.
- First derivative of mass loss (DTG). Its maximum tells us the highest degradtion temperature point.
- Gram-Schmidt signal (GS). Different from the prevoius two, it comes from the coupled IR spectrometer and it encodes the total IR absorption due to gaseous by-products as temeprature increases.

2.3 Notes on handling and reproducibility

- Every air-/moisture-sensitive manipulations (weighing, loading the milling jar, loading pellet dies) were performed inside an Ar-filled glovebox to minimize unwanted oxidation.
- Despite careful handling, some brief exposure to ambient atmosphere occurred during pellet pressing and during optical/XRD measurements performed on non-atmosphere-controlled instruments.

Chapter 3

Results and discussion

In this chapter we're going to discuss the results of synthesis and characterization of target materials in this thesis: $DMASnI_3$ and $DMASnBr_3$ perovskites. For both compounds we are going to first talk about mechanochemical synthesis results through XRD and UVVis spectra. Here all the measurements have benn carried out on pellets form. Afterwards, a deeper analysis on the enviromental effects is provided and discussed thanks primarly to in-situ XRD characterizations. In the latter part, we are going to focus on the role of agents such as oxygen, air and water. Regarding the iodide compound only, FESEM images are provided with respect to relevant environmental conditions , while a more detailed analysis will be held about thermal stabilty through thermogravimetric analysis. Lastly, thin films behaviour with respect to powder samples in both air and high humidty environments is going to be explored and comented qualitatively.

3.1 $DMASnI_3$

3.1.1 Synthesis result

The mechanochemical synthesis of $DMASnI_3$ was successfully carried out by ball milling as specified in Section 2.1. After 40 minutes of milling the reaction yielded a pale-yellow powder (Fig. 3.1a), in agreement with the literature [3,51,52]. Samples collected within shorter milling times (10, 20 and 30 minutes) exhibited the same coloration, indicating that the product already forms at early stages of the reaction. From these intermediate aliquots, pellets were also prepared (Fig. 3.1b). Compared to the loose powders, pellets appear orange in colour; this should not be attributed to a different composition, but rather to the enhanced optical absorption caused by powder densification during pressing. Moreover, darker areas are visible within some pellets. This heterogeneity it may be attributed to the material's intrinsic air sensitivity and it may arise from partial oxidation of Sn^{2+} to Sn^{4+}. Indeed, once exposed to air, the yellow powder gradually darkens within 20–30 minutes until it turns completely black; therefore, the darker regions observed are likely the result of powder exposure to air during pressing, as anticipated in Materials and Methodology, Section 2.1). This behaviour though it's not new and it is consistent with previous reports in the literature [51,52].

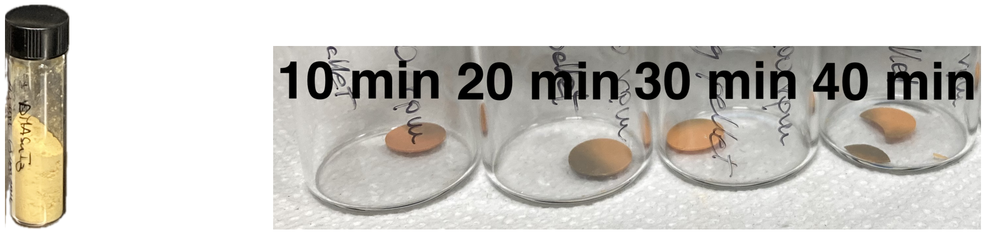

(a)

(b)

Figure 3.1: **Panel (a):** synthesised pristine $\mathrm{DMASnI_3}$ in glovebox. **Panel (b):** pellets obtained at different milling times.

The phase purity of the product was assessed by X-ray diffraction. The diffraction patterns of pellets obtained after 10, 20, 30 and 40 minutes of milling are virtually indistinguishable (Fig. 3.2). All samples show a good match with the reference pattern reported in the literature [3], confirming the formation of the targeted phase already after 10 minutes of milling. No relevant differences were observed in peak intensity or broadening, suggesting that crystallite size and structural quality are not significantly affected within this reaction time window. While extended milling times could in principle lead to finer powders, a total duration of 40 minutes was chosen as a practical compromise.

UV–Vis reflectance spectra collected on the pellets (Fig. 3.3) are not perfectly homogeneous due to the aforementioned inhomogeneous pigmentation of the samples. The fact that we clearly observe darkening in the UV–Vis spectra but not in XRD suggests that the oxidation of tin is — at least in these conditions — primarily superficial and amorphous, thus undetectable by X-ray diffraction.

The UV–Vis spectra reveal a clear absorption onset between 500 nm and 600 nm, which can be assigned to the fundamental band gap of $\mathrm{DMASnI_3}$. A second increase in absorption is observed at wavelengths approaching 900 nm, likely due to the darker regions mentioned above. This feature is better highlighted by inspecting the reflectance spectrum of the air-exposed pellet sample (Fig. 3.4), where the curve starts to increase only after 800 nm. Unfortunately, we cannot further investigate the small band gap because the spectrometer we used covers only the 300–900 nm range.

Energy band-gap values have been estimated from the UV–Vis spectra and are reported in Table 3.1, giving a mean value of $E_g = 2.3175$ eV, close to values reported in the literature ($E_g = 2.36$–2.48 eV) [51,52]. In 2018 Ju et al. synthesised and investigated the chromogenic behaviour of $\mathrm{DMASnI_3}$ single crystals. They

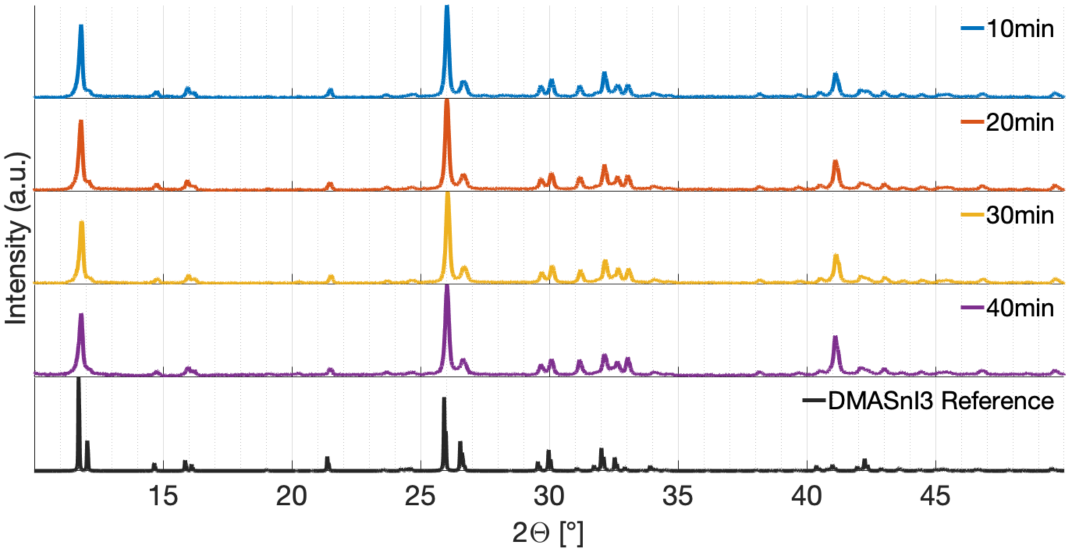

Figure 3.2: XRD (@DISAT) milling cycle comparison of DMASnI$_3$ pellet (Fig. 3.1b) samples with the crystallographic reference.

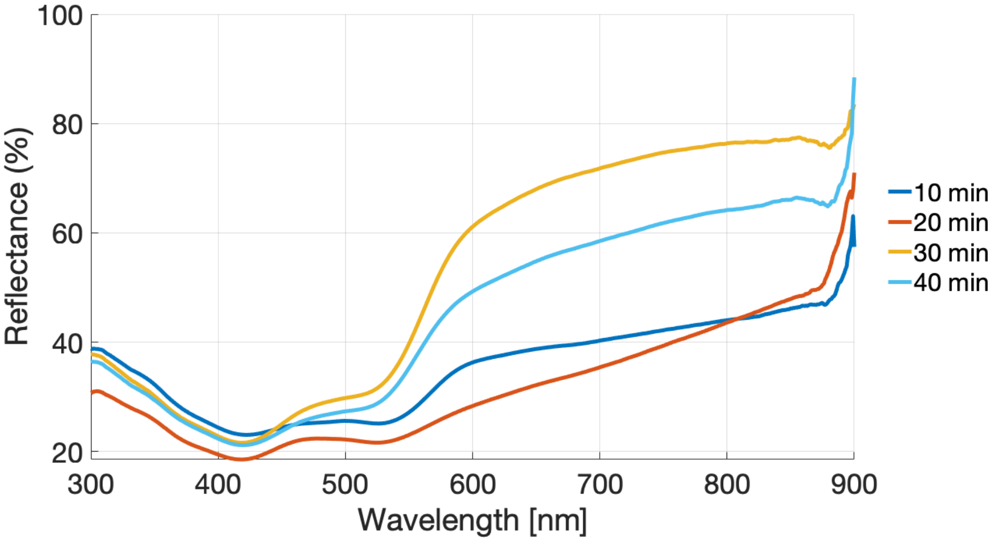

Figure 3.3: UV–Vis reflectance spectra of DMASnI$_3$ pellets at different milling times.

refer to the air-exposed crystal as the "black phase", in contrast to the pristine "yellow phase". Their UV–Vis experiment revealed that yellow phase exhibits a band gap value of 2.48 eV (in reasonable agreement with a first-principles calculation predicting 2.77 eV [61]), whereas their black phase exhibits a value of 1.32 eV. This latter value likely corresponds to the second onset observed at long wavelengths in

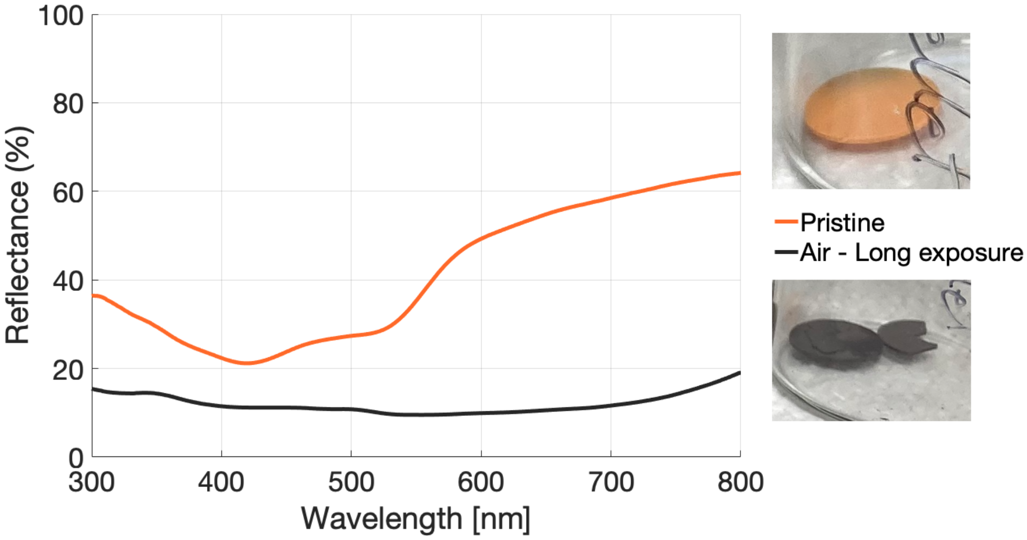

Figure 3.4: UV–Vis reflectance spectra of DMASnI_3 pellets from the 40-minute milling time ("Pristine”, blue solid line) and overnight air-exposed sample ("Air-Long exposure" yellow solid line).

Table 3.1: Band-gap values for DMASnI_3 pellets estimated from the reflectance spectra at different milling times.

Sample (milling time)	10 min	20 min	30 min	40 min	**Average**
Estimated E_g	2.29 eV	2.33 eV	2.34 eV	2.31 eV	2.3175 eV

our samples, i.e. below $\sim 900\,\text{nm}$ i.e. 1.4 eV.

3.1.2 In-Situ environmental tests

From previous observations made after synthesis and pellet making, this compound is sensitive to air, therefore our goal is to understand, crystallographically speaking, how air is responsible for the colour change and how the "black phase" can be classified. Interested by the unique chromogenic behaviour, we continue our investigation by collecting and comparing the crystalline phases of DMASnI$_3$ under different atmospheres (N_2, O_2, air, water) to characterise its stability. In Fig. 3.5 are summarised what we found to be the key phases of DMASnI$_3$ with respect to experimental conditions. Starting from the pristine condition (Fig. 3.5(a)), the powder sample was introduced into the XRD measurement chamber while maintaining inert conditions. A close-up between the experimental diffraction pattern acquired under inert condition and the crystallographic reference is shown in Fig. 3.6, confirming that the pristine material is phase-pure and therefore setting a baseline for further set of measurements. Togheter with diffraction pattern, FESEM pictures of the pristine sample has been taken (Figs. 3.7), highlighting a sort of honeycomb pattern, with irregular features raging from over hundreds to tens of nanometers.

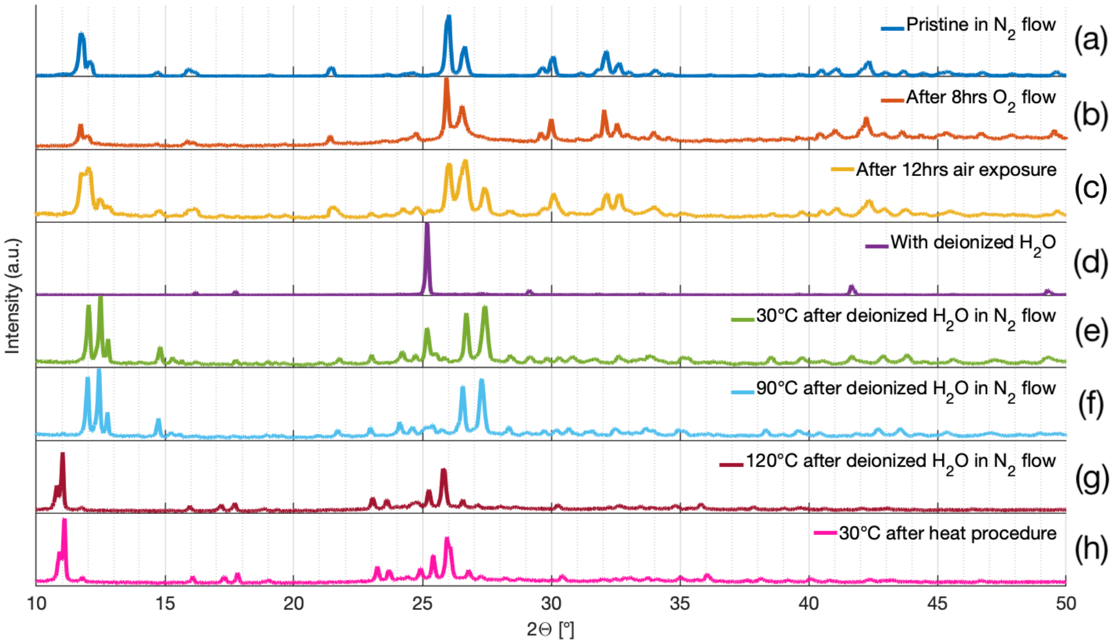

Figure 3.5: XRD patterns (acquired at @IIT-CCT, Genoa) of the most relevant phases observed during in-situ measurements of DMASnI$_3$ powder. Chronologically, the patterns are shown top to bottom, starting from the pristine condition **(a)**, oxygen only exposure **(b)**, ambient air exposure **(c)**, de-ionized water **(d)**. Panels **(e)**,**(f)**,**(g)** and **(h)** instead represent a summary of a longer heat experimental test conducted after water expsoure. Each pattern is discussed in detail later on.

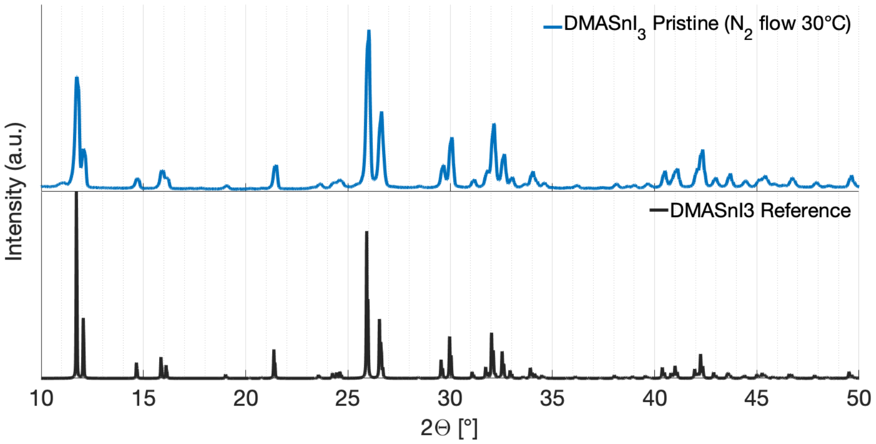

Figure 3.6: Close-up of the XRD pattern of $DMASnI_3$ powder measured under inert N_2 atmosphere, compared with the crystallographic reference (COD: 96-810-3986 [3]).

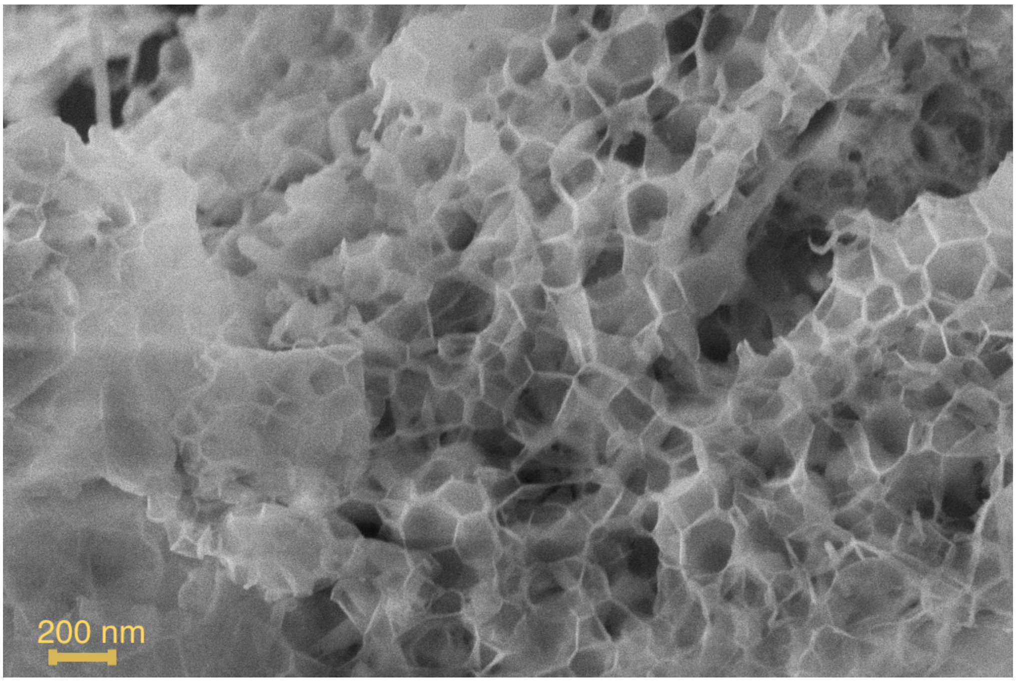

Figure 3.7: FESEM pictures of pristine $DMASnI_3$. Set-up: WD=4.8 mm; Magnification=30Kx.

From the pristine phase it begins our study of how environmental agents may affect $DMASnI_3$. We have already anticipated and discussed how air clearly has effects on our samples while commenting the synthesis results, nevertheless, we took an extra step before exposing directly the sample to ambient air: we first exposed the measurand to oxygen alone, since it is plausible that dimming in colour is due to oxidation. Our goal is to compare the effect of oxygen alone with air, i.e. O_2 and humidity togheter. That being said, the sample was exposed to a continuous pure O_2 flow for 8 hours at room temperature and diffraction patterns were acquired every 45 minutes. Taking a glance at the pristine phase and the last acquired pattern, i.e. after 8 hours of air, no substantial changes are visible (Fig. 3.5(a)-(b)). A more detailed look at the intermediate patterns though (Fig. 3.8) reveals instead a gradual decrease of intensities as oxygen continues to flow along the entire spectrum. Although this evidence openly suggests an amorphous transition of the material, we cannot establish whether and which new non-crystalline species, therefore not detectable via XRD, were formed. Along with the observed amorphization and consistent with the prior chromatic behaviour in air, the powder steadily darkened, turning completely black after prolonged O_2 exposure (Figs. 3.9a and 3.9b). FE-SEM images of the oxygen exposed sample is shown hereafter (Fig. 3.10). We can observe, with respect to the pristine one (Fig. 3.7), that the morofology is somehow reminescent of the previous observed "alveoli" pattern, but in a rougher and larger appereance, indicating that oxygen has reacted with the sample decreasing cristallinity as the relative XRD is suggesting us.

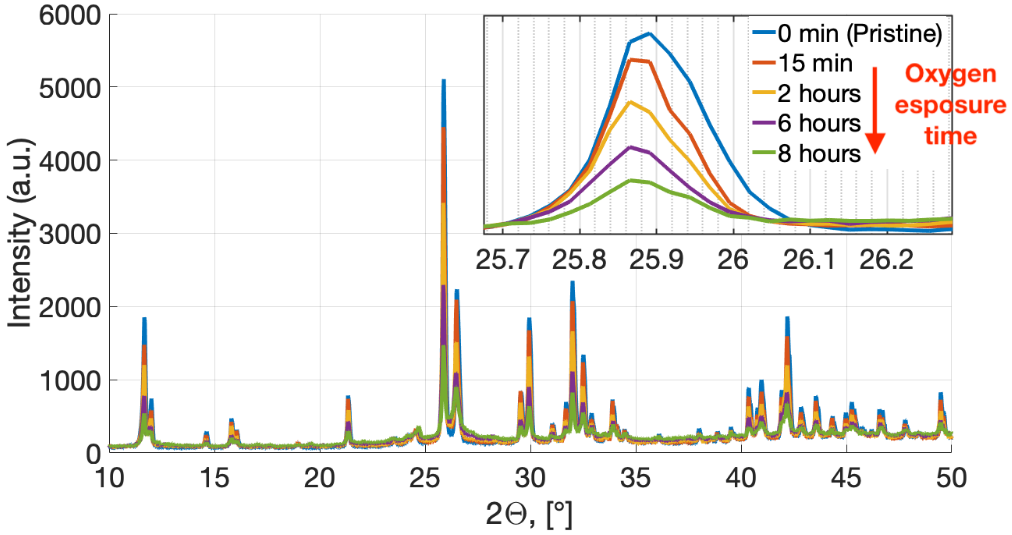

Figure 3.8: Evolution of the XRD pattern of DMASnI$_3$ powder during 8 hours exposure to O_2. The patterns overlap in peak positions but gradually decrease in intensity.

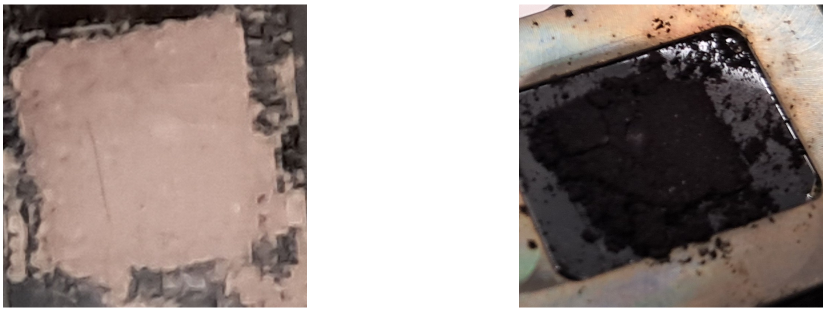
(a) (b)

Figure 3.9: Photographs of $DMASnI_3$ sample **(a)** before and **(b)** after oxygen exposure.

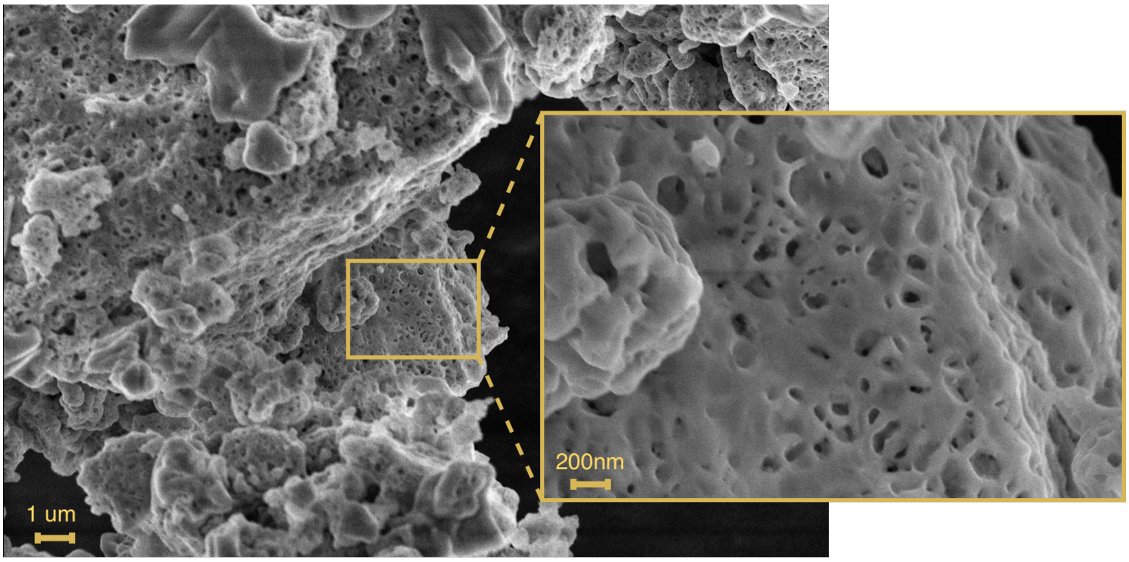

Figure 3.10: FESEM image of oxygen exposed $DMASnI_3$ sample with relative zoom in a constrained area. Set-up: WD=3.9 mm; Magnification=5Kx (30Kx for the close-up).

When the O_2-treated sample was subsequently exposed to ambient air (R.H. $\sim$ 55%) for 12 hours, its diffraction pattern clearly changed, as shown in Fig. 3.11. New reflections marked with black star ($\star$) symbol are highlighted and appear most notably at $2\Theta \sim 12^\circ$, $\sim 24^\circ$ and $\sim 27^\circ$, which are not indexed to the pristine phase. This provides direct evidence that oxygen alone is not sufficient to trigger the observed crystalline rearrangement; rather, both oxygen and water (acting as a catalyst) are required. Red triangle (▼) labels indicate instead the (main) reflections that are comparable with the pristine phase and still are present in the new air phase. Interestengly these are similar to those reported by Li et al. (2024) after solvothermal treatment of DMASnI$_3$ crystals [4]. In this study they reported a novel phase, denoted as DMASnI$_3$(O), obtained by oxygen surface reconstruction. A strong correlation is observed between XRD pattern of DMASnI$_3$(O) (Fig. 3.12) and what we observed as the pattern of DMASnI$_3$ after air-exposure. DMASnI$_3$(O) phase has been proved to have excellent catalytic selectivity over CO_2 reduction in ethylene and long water stability. Although the promising matching between our

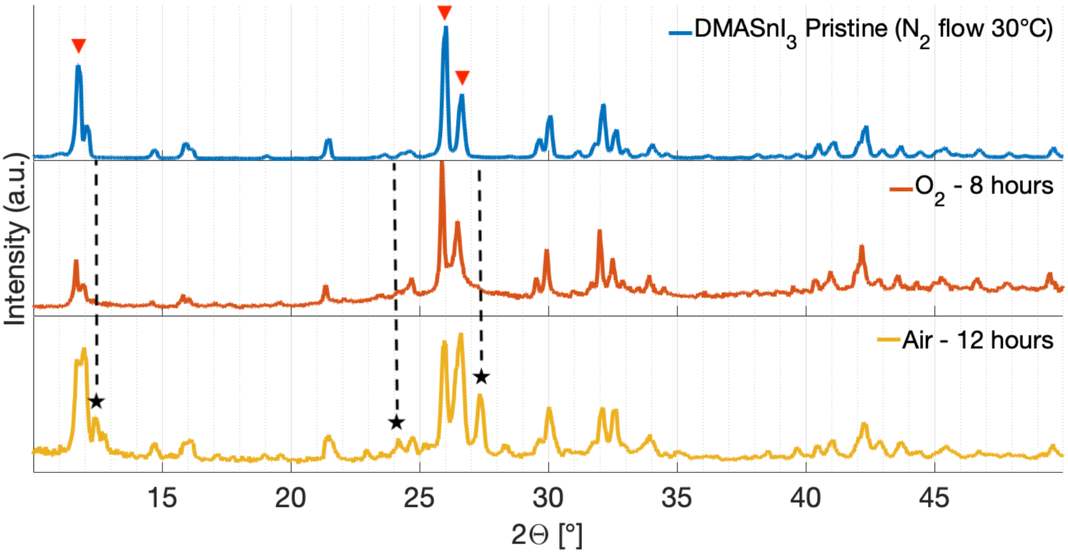

Figure 3.11: XRD pattern of pristine DMASnI$_3$ powder, after 12 hours of O_2 and after 12 hours of air. The black star (⋆) symbols highlight new reflections arising after air exposure, comparable with DMASnI$_3$(O).

air phase and DMASnI$_3$(O), due to different synthesis paths specifically in reaching the oxiginated phase, it is likely expected to not show the same photocatalytic performances as reported by Li et al. FESEM pictures of an air exposed sample (Fig. 3.13) show a similar morfology to the oxygen exposed sample (Fig. 3.10), with the same superficial strucutres and sized features. Therefore in order to better explore this correlation and its characteristics, additional measurements such as electron dispersive X-ray spectroscopy (EDS), Raman spectroscopy and of course photocatalytic reduction test would be required.

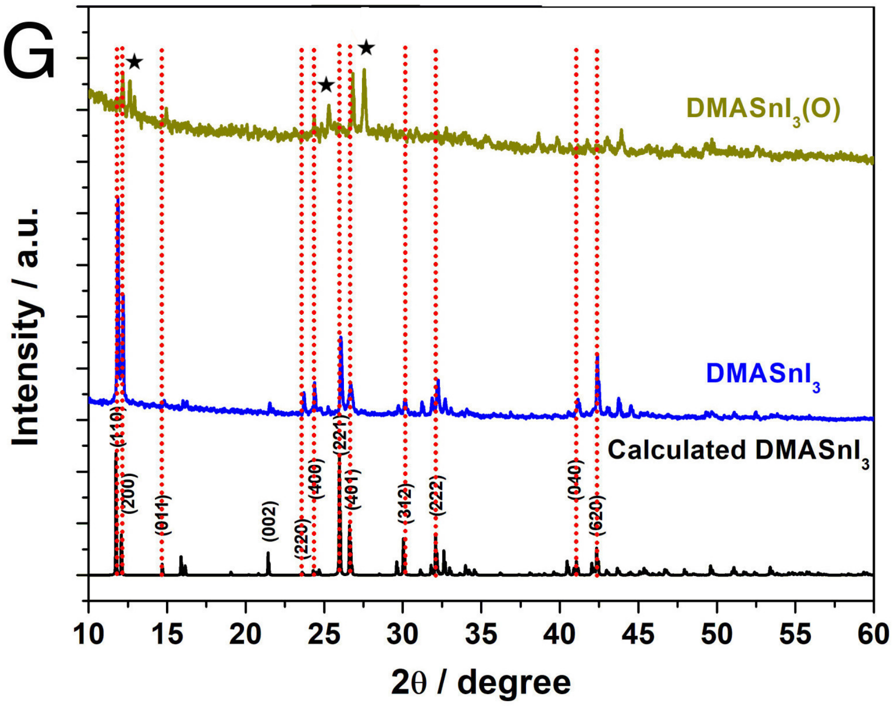

Figure 3.12: XRD pattern of $DMASnI_3(O)$, reproduced from Fig. 1.G of Li et al. [4]. Dashed red lines depict already known reflections from the pristine phase ($DMASnI_3$). Black star (⋆) symbols denote reflections of the *surface-reconstructed phase* $DMASnI_3(O)$ and are compared with those of the air-exposed $DMASnI_3$.

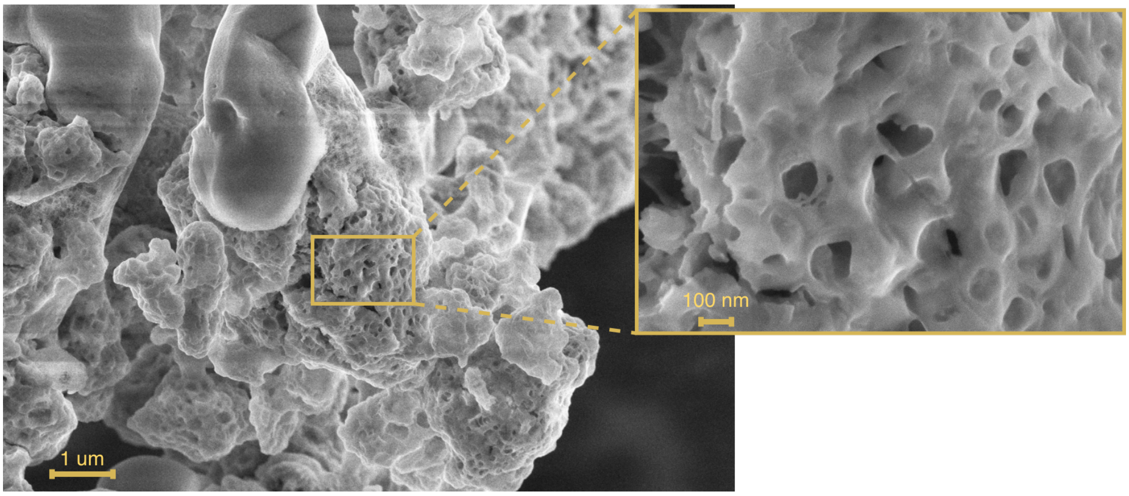

Figure 3.13: FESEM image of oxygen exposed $DMASnI_3$ sample with relative zoom in a constrained area. Set-up: WD=4.2 mm; Magnification=10Kx (70Kx for the close-up).

We then investigated the material's stability in contact with water, continuing from the air-exposed powder sample. Ju et al. [51] reported that DMASnI$_3$ crystals transition from yellow to black upon air exposure and that the black phase can revert to yellow when wetted with water. They described a cycle:

Yellow (Inert) → Black (Air) → Yellow (DI water)

suggesting that the pristine phase can be restored from the air-exposed one. Their conclusion is mostly supported by correlations among XRD patterns of the phases above (yellow, black, yellow after DI water). In our experiments, when the degraded powder was wetted with deionized water the colour immediately switched back from black to yellow (Fig. 3.14), as expected. However, the XRD pattern acquired immediately afterwards (Fig. 3.15) revealed a strong crystalline presence of SnI$_4$, with its main reflection at $2\Theta \sim 25°$. This indicates that water accelerates oxidation of Sn^{2+} to Sn^{4+}, yielding decomposition products and, in our conditions, contradicting the simple reversibility reported previously.

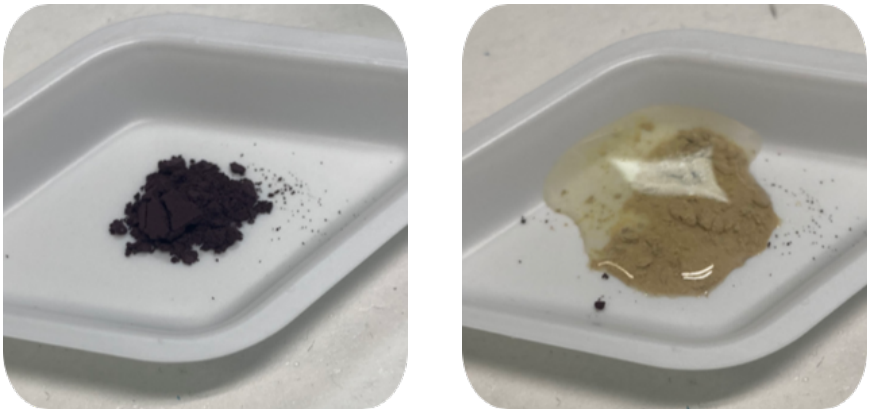
(a) (b)

Figure 3.14: Pictures of DMASnI$_3$ powder **(a)** before and **(b)** after hydration.

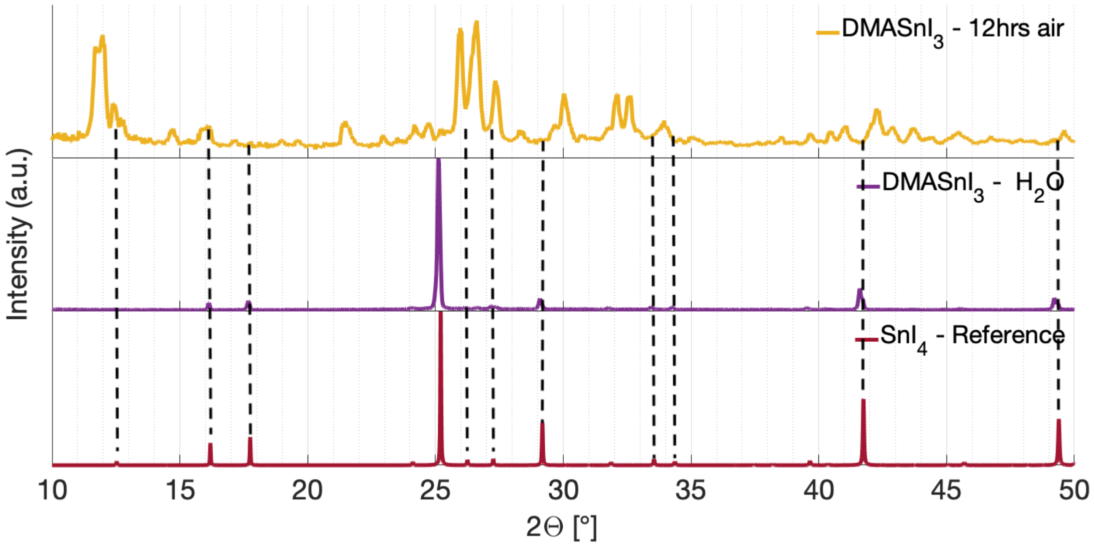

Figure 3.15: XRD pattern of DMASnI$_3$ powders before and after exposure to deionized water, compared with the reference pattern of SnI$_4$ (COD: 1010610 [5]).

Figure 3.16 show FESEM images of DMASnI$_3$ powder after water exposure (and dried in air at room temperature overnight). Here we can appreciate substantial changes with respect to the air exposed sample, the morfology is completely changed with large grains and features showing up as product of water reaction with the powder. These effects are even more accentuated in a second image (Fig. 3.17) where huge grains and feature can be appreciated, probably due to SnI$_4$ presence as highlighted by the relative diffraction patterns.

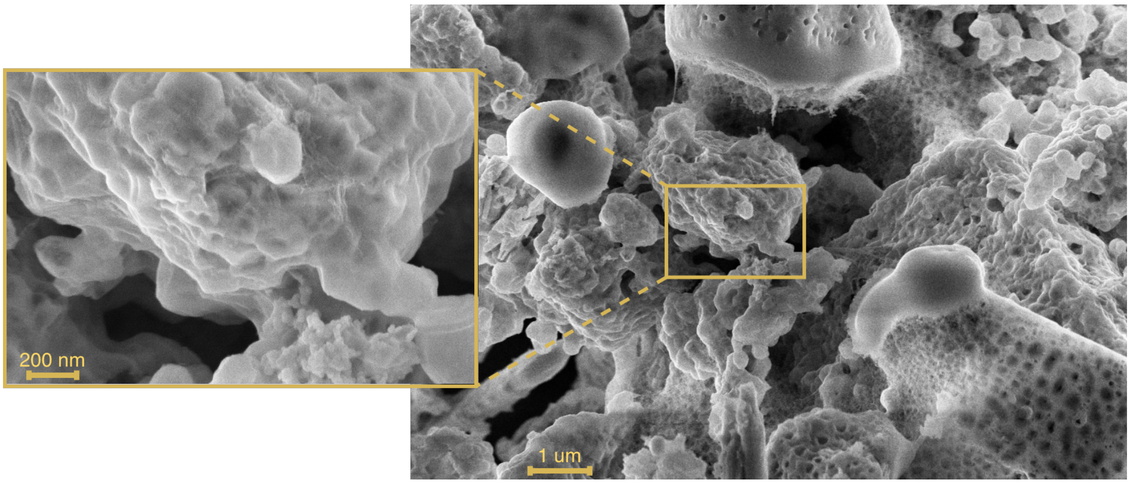

Figure 3.16: FESEM image of water exposed DMASnI$_3$ sample with relative zoom in a constrained area. Set-up: WD=4.2 mm; Magnification=10Kx (50Kx for the close-up).

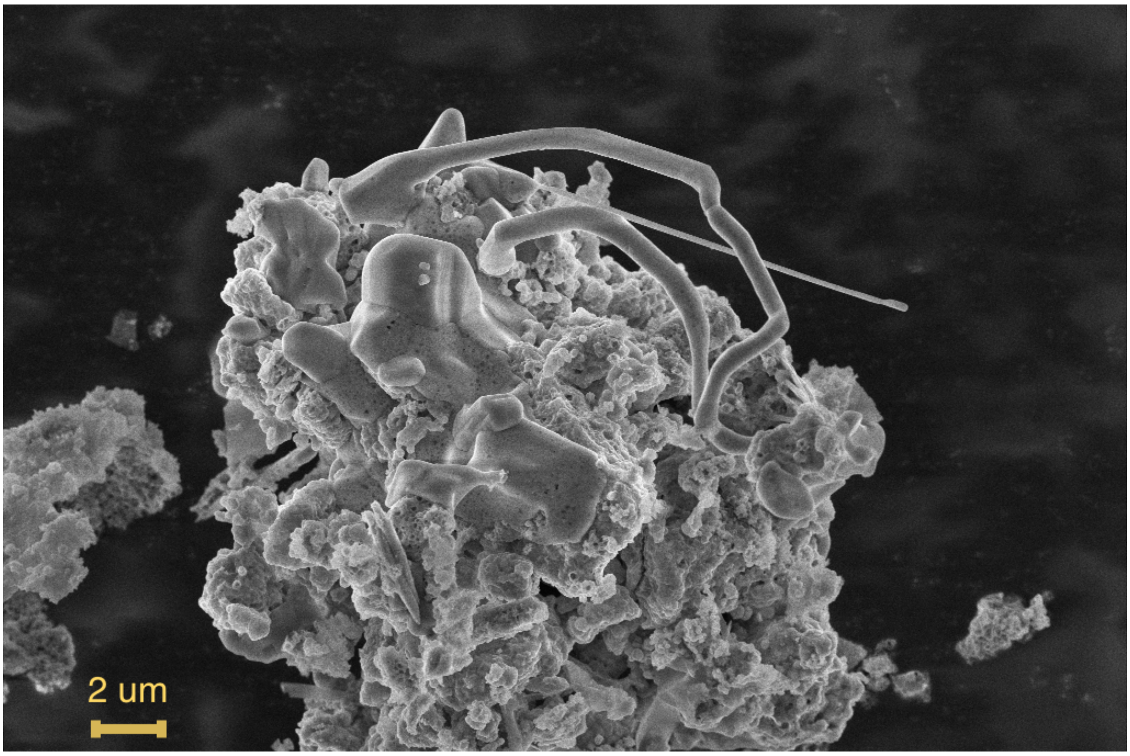

Figure 3.17: FESEM image of water exposed DMASnI$_3$ sample. Set-up: WD=3.9 mm; Magnification=3.21Kx.

To further probe the reversibility condition, wetted sample was dried under continuous N_2 flow and heated up to 120°C and then cooled back to room temperature. Patterns were acquired every 45 minutes during the treatment. At each acquisition interval it corresponds a temperature increasing of +20°C . By doing that we attempted to favour the removal of oxidizing agents, i.e. air and water molecules through N_2 flow and thermal agitation, in order to recover the pristine phase. Figure 3.18 contains the spectra collected during this experimental procedure, together with the air-exposed and pristine spectra for reference. Dashed lines, red star (⋆) and black square (■) symbols are related to air-exposed and pristine phase peaks, respectively. These labels have been added to emphasise differences and to ease comparison among phases. Plots within the double blue arrow labelled "N_2 flow" are the actual diffraction patterns measured during heating. The angular range has been limited to $10° < 2\Theta < 30°$ since the most relevant feature changes occur in this interval.

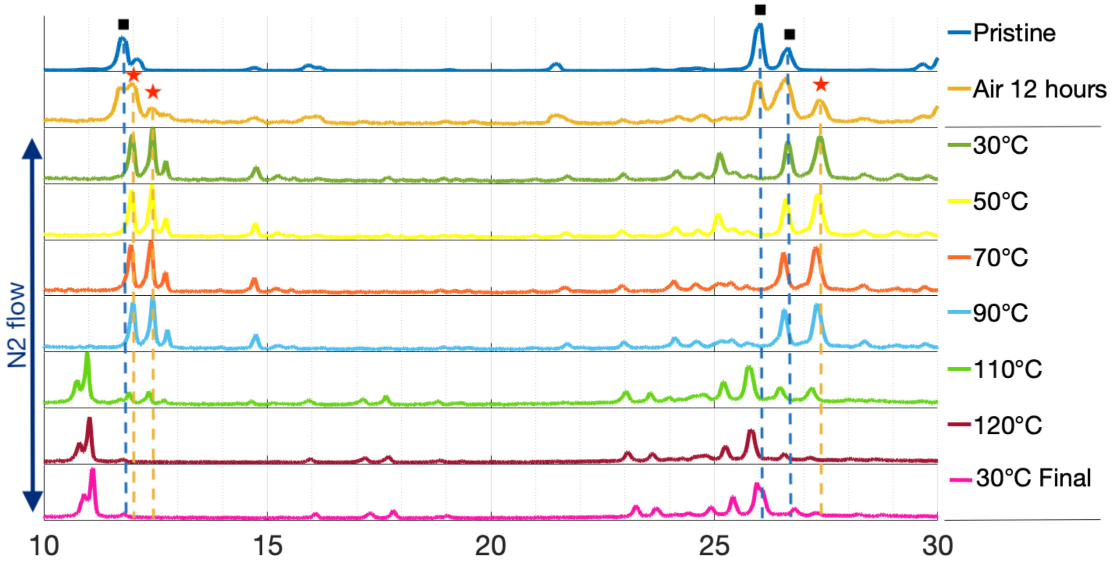

Figure 3.18: XRD spectra collected during the heat treatment after DI water exposure.

First, the diffraction pattern collected under N_2 flow at room temperature (30°C) after water exposure (Fig. 3.18) exhibits a different pattern from the one observed immediately after water (Fig. 3.15). It is noteworthy how it resembles a superposition of the characteristic SnI_4 peak ($2\Theta \gtrsim 26°$), peaks from the pristine phase (■) and other peaks that emerge in air (⋆). This suggests that, upon drying, the powder reveals a mixture of several phases rather than a single pure crystalline phase.

As temperature increases, up to about 90°C (Fig. 3.18), two main effects are observed: first, lattice expansion due to temperature causes a slight negative shift of all peaks (more evident in the rightmost labeled peaks), secondly, the peak associated with SnI_4 gradually decreases in intensity.

A more pronounced transformation occurs above 90°C (Fig. 3.18): the rightmost labelled peaks (⋆ and ■) diminish while a peak associated with the pristine phase (■) reappears. Meanwhile, the pair of peaks at the left (⋆) also fade and are replaced by new, previously unrecognised reflections at lower 2Θ. This transformation appears to persist after cooling back to room temperature (Fig. 3.18(g)). It is important to note that the abrupt crystal change above 100°C is most likely associated with degradation of the organic cation. In addition, the sample colour turned black again after drying due to the high temperature reached (Fig. 3.20a).

Concluding this section, we wanted to spend some words about the reversibility claimed by Ju et al. in 2018 [51]. Through our experiments we were able to reproduce the phases present in their work: yellow(pristine), black(air) and wet black (after H_2O). A summary of the latter phases (pristine, air, and after DI water) is shown in Fig. 3.19 where it is possible to observe many discrepancies among the phases. First of all we have already discussed how air is affecting the crystal strucutre of the pristine phase and therefore how these two phases are equivalent, secondly, the after water pattern exhibits divergences from the air exposed one: many peaks associated with the pristine phase are missing (see ▼) while other peaks, even from the air phase (see ⋆), change in amplitude. Last but not least, a rather sharp peak (see SnI_4) is clearly telling that after water exposure the compound is reminiscent of its crystal structure in water, i.e. strongly correlated with SnI_4.

Figures 3.20a and 3.20b show photographs of the sample after drying in N_2 flow and after the full heat procedure plus five days of air exposure, respectively.

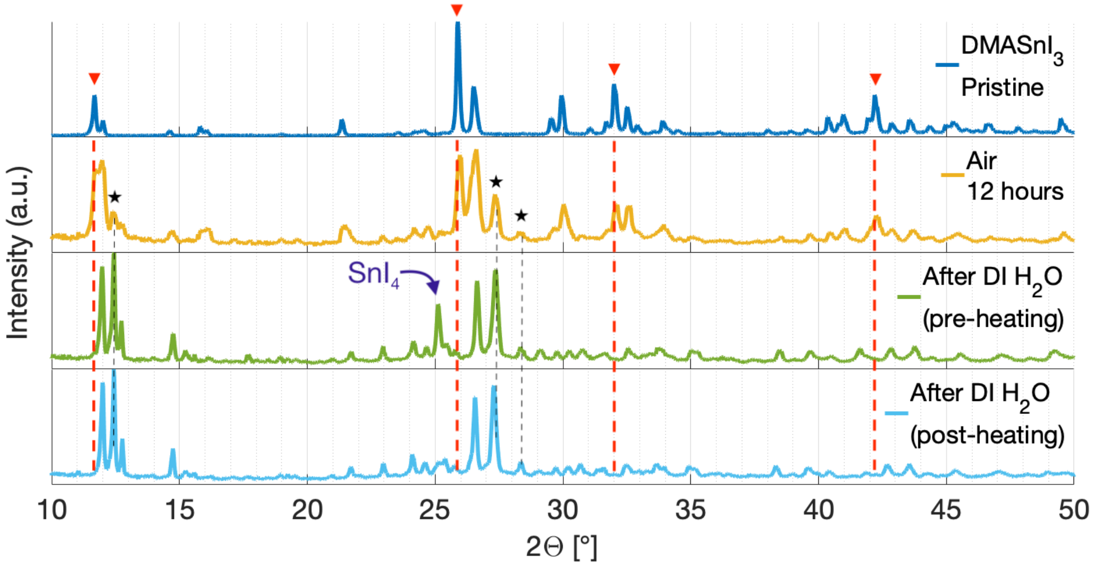

Figure 3.19: XRD patterns of DMASnI$_3$ for the three phases: pristine, air-exposed and after water exposure (pre-heating). Red triangles (▼) inidcates pristine phase peaks that are not retained after DI H_2O. Black stars (⋆) instead depict the characteristic peaks of the air phase that are present after water too.

(a)

(b)

Figure 3.20: **Panel (a):** DMASnI$_3$ sample right after drying in N_2 flow at 30°C. **Panel (b):** DMASnI$_3$ sample after the post-water treatment (N_2 and heating).

3.1.3 Thermogravimetric analysis results

To assess temperature stability, two thermogravimetric analyses were carried out on ∼30 mg DMASnI$_3$ powder samples: one “pristine” sample (inserted directly from the glovebox into the crucible and kept under continuous N_2 flow) and one “air-exposed” sample (previously exposed to air and kept under ambient-air flux). Both samples were tested between room temperature (∼ 27°C) and 800°C. We will refer to the two measurements as “N_2” and “Air”, respectively. Values of the onset temperature are displayed in Table 3.2.

Table 3.2: Estimated onset temperatures from the TGA experiments on DMASnI$_3$. The "N$_2$" label refers to the sample that was never brought into contact with air.

Experimental flow	N$_2$	Air
Onset T	314 °C	186 °C

Figures 3.21 and 3.22 show the signals acquired during TGA as a function of temperature: the mass loss (in percentage), the corresponding derivative DTG (dM/dT) and the Gram–Schmidt (GS) signal.

It is immediately apparent how the two experiments differ: the onset temperature changes significantly, with the air-exposed sample showing a much lower onset than the pristine one. This result is consistent with the post-water heat treatment and the observed crystalline degradation above 100°C. In particular, the air-exposed sample shows a pronounced release of volatile species between 100°C and 140°C (see the GS signal in Fig. 3.22).

The pristine sample shows a higher onset temperature (possibly due to higher crystallinity), and also exhibits two distinct DTG peaks, which are often associated with two different degradation mechanisms. Since the sample is an organic–inorganic compound, it is plausible that the first peak corresponds to degradation of the organic part (DMA cation or residual ammonium species), while the second peak is related to the inorganic component (Sn–I framework).

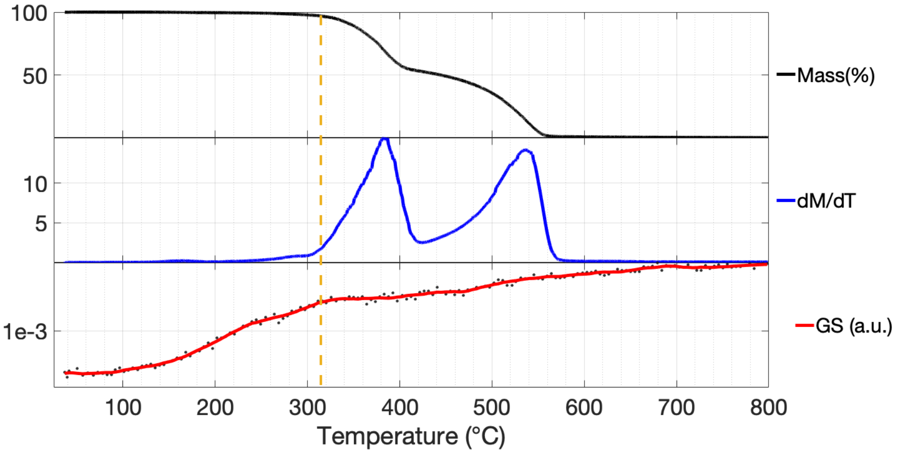

Figure 3.21: TG, DTG and GS curves as a function of temperature for the pristine sample kept under continuous N$_2$ flow. Dashed orange line represents the onset temperature at 314°.

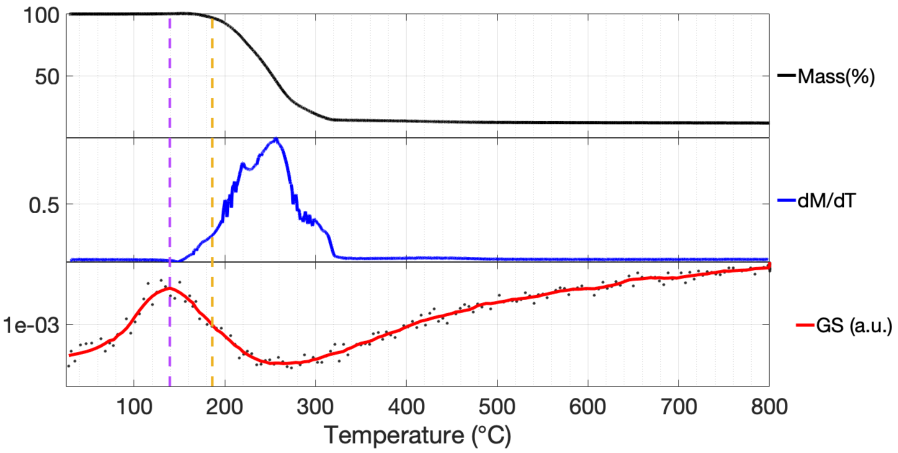

Figure 3.22: TG, DTG and GS curves as a function of temperature for the air-exposed sample. Dashed purple line represents the maximum recorded GS signal at 139°, while the orange one represents the onset temperature at 186°.

3.1.4 Thin films

The DMASnI$_3$–1-butanol solution appeared as a yellow opaque liquid (Fig. 3.23a), indicative of partial dissolution and dispersion of the powder in the alcohol medium. Upon spin coating and drying, the as-deposited films exhibited a violet colouration (Fig. 3.23b), consistent with the visual appearance of the powdered material when dried from an aqueous suspension. However, a progressive colour evolution was observed when the films were exposed to ambient atmosphere. Slower than for the powder, the films transitioned from violet to yellow (Fig. 3.23c). This phenomenon, not fully understood at the present stage, suggests that air exposure — most likely a combination of oxygen and humidity, as already indicated by the in-situ powder

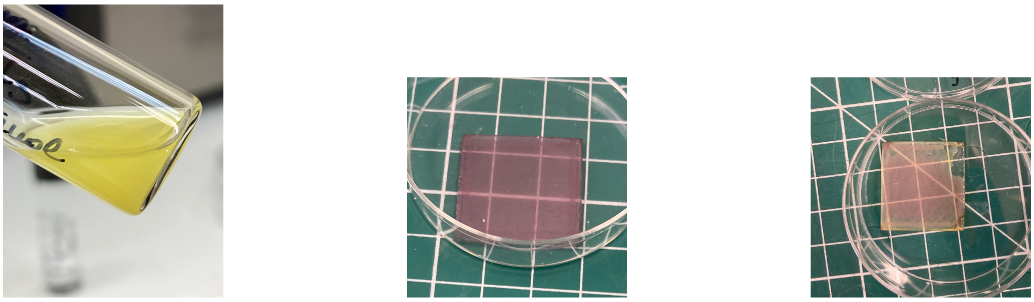
(a) (b) (c)

Figure 3.23: Pictures related to thin-film preparation and ageing: **(a)** DMASnI$_3$ in 1-butanol (solution), **(b)** spin-coated thin film stored in glovebox, **(c)** thin film stored in ambient air for three days after deposition.

XRD — plays a critical role in initiating structural or chemical transformations. A control experiment confirmed this hypothesis: a film stored in a glovebox under inert atmosphere (Ar) remained stable, without detectable colour change, indicating that the degradation process is triggered by the external environment. This observation aligns with literature reports and with our own prior investigations on DMASnI$_3$ powders. Based on these considerations, we hypothesise that thin films, due to their higher surface-to-volume ratio, might be even more prone to such environmental reactivity. To further investigate the role of humidity, an experiment was performed in which a film was exposed to a highly humid environment (R.H. $> 80\%$). To do so, a beaker with water was heated just below its boiling point to increase the relative humidity within a confined volume. The film was then manually suspended above the hot water vapour. A shematic represenation of this set-up is showed in figure 3.24 Under these conditions, the film showed accelerated colour transitions from dark violet to bright yellow; when the film was moved away from the high-humidity environment the dark colour was restored, confirming the catalytic role of water molecules in its optical and structural change. This experiment also reinforced the idea that while DMASnI$_3$ films may initially preserve a perovskite-like appearance, their stability under ambient conditions is severely limited. These findings underline both the potential and the challenges of processing DMASnI$_3$ via green solvents such as butanol. On one hand, the approach demonstrates the feasibility of depositing films without resorting to toxic solvents; on the other hand, the material's instability under ambient conditions highlights the necessity of further optimisation strategies, such as encapsulation, compositional engineering or protective processing environments.

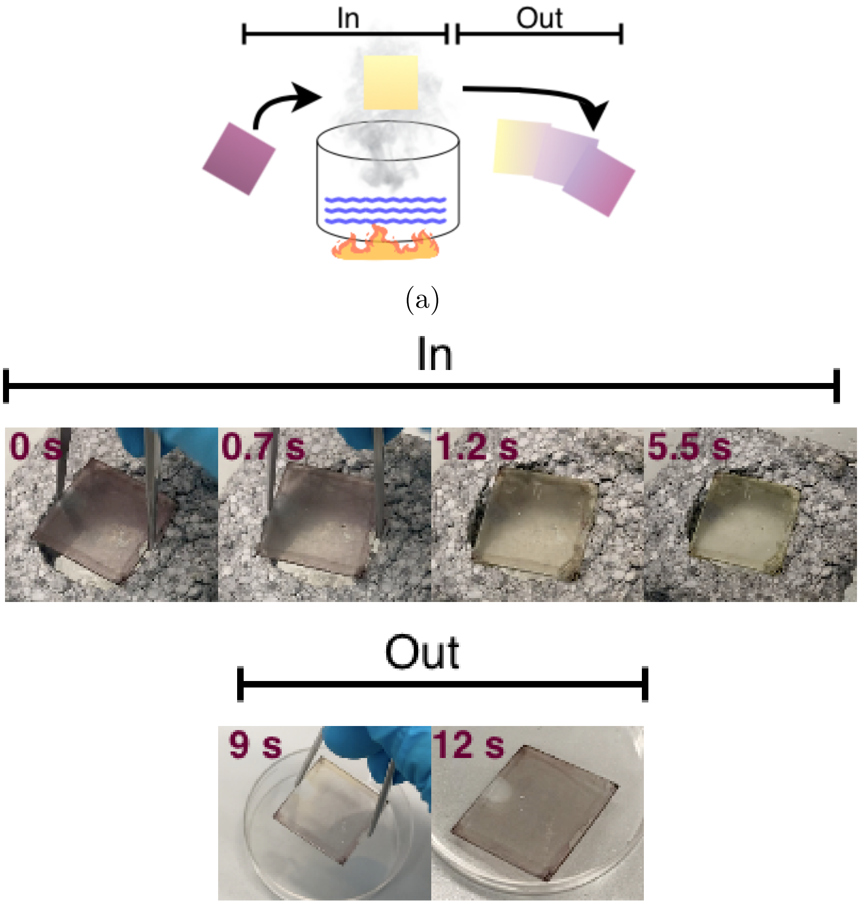

(a)

(b)

Figure 3.24: **Panel (a):** Schematic representation of the experimental setup used for qualitatively investigating humidity effect on $DMASnI_3$ (1-butanol) thin films. **Panel (b):** Pictures of the thin film during the actual experiment.

3.2 $DMASnBr_3$

3.2.1 Synthesis result

Results of the he mechanochemical synthesis of $DMASnBr_3$ are similar to the iodide counterpart. Same method has been carried out, i.e. 40 minutes of milling at 400rpm with aliquots sampled every 10 minute interval. The so formed final powder is presenting itself in a bright yellow color (Fig. 3.25a), while pellets (Fig. 3.25b) shows color closer to orange, again as discussed in the $DMASnI_3$ section, a darker color is due to pressed powder that enhance the dispersion of light. Unlike $DMASnI_3$, we don't observe any radical color change when the powder is exposed to air.

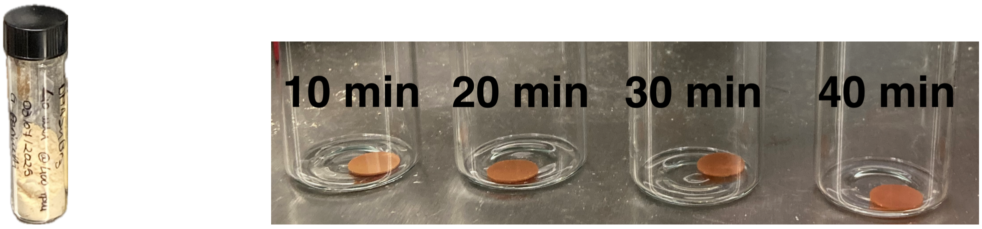

(a) (b)

Figure 3.25: **Panel (a):** synthesised pristine DMASnBr$_3$ powder (stored in glovebox). **Panel (b):** different milling time pellets of DMASnBr$_3$.

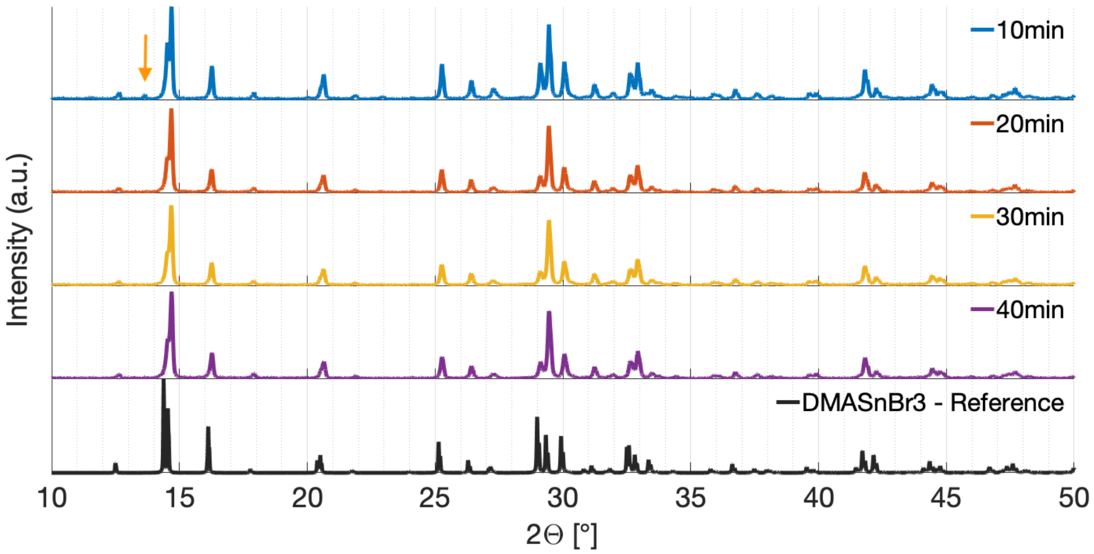

Figure 3.26: XRD cycle comparison of DMASnBr$_3$ with crystallographic reference (COD:96-810-3984 [2]). The orange arrow represents the unknown reflection that appears only in the 10 min sample for disappearing later on.

XRD patterns of the milling sample are shown in Fig. 3.26. Obtained pattern after 10 minutes already exhibit the characteristic reflections of the perovskite structure and remain essentially stable over longer milling times. The only notable difference with respect to the other is contained in a minor reflection at $2\Theta \approx 13.5°$. Initially, this additional reflection was tentatively ascribed to unreacted precursors (DMABr or SnBr$_2$).

However, a direct comparison with their reference XRD patterns (Fig. 3.27) excludes this possibility, as no correspondence is observed. Furthermore, the peak appears with relatively low intensity, reinforcing the hypothesis that it does not originate from residual precursors but rather from a minor secondary phase or from a structural artefact. Overall, the good agreement with the reference pattern

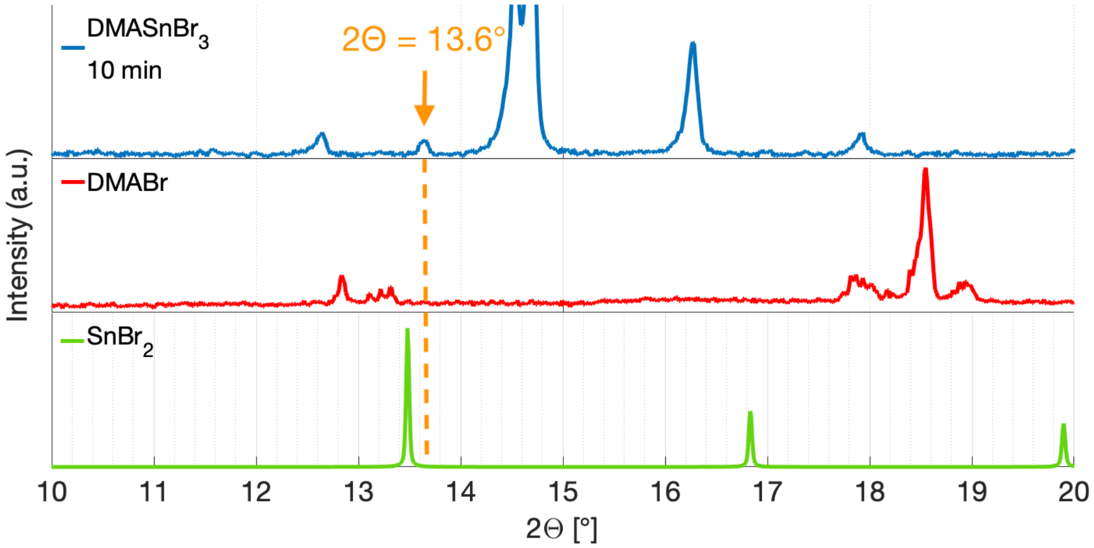

Figure 3.27: Detail of the XRD pattern of DMASnBr$_3$ 10 minute sample from figure 3.26, compared with crystallographic references of the precursors DMABr (measured from our precursor) and SnBr$_2$ (ICSD: 411177 [6]). The orange arrow represent the investigating reflection point.

confirms the successful synthesis of DMASnBr$_3$.

Figure 3.28 reports the UV-Vis reflectance spectra acquired on DMASnBr$_3$ pellets at different ball-milling times (10, 20, 30 and 40 minutes). The spectra are highly comparable among each other, displaying a smooth absorption edge typical of a direct band gap semiconductor. The only noticeable deviation is observed for the 10-minute sample, which shows a slight difference in its spectral profile with respect to the other cycles. This feature can be imputed to the small additional reflection described earlier in the corresponding XRD pattern (3.26). Regarding the rest of the samples (20, 30, 40 minutes), optical spectra overlap almost perfectly suggesting that the perovskite phase is fully formed already after the first 15-20 minutes of grinding. Band-gap values estimated from the UVVis spectra are shown in table 3.3.

Table 3.3: Band gap values estimated from the reflectance UVVis plots.

Sample (milling time)	10 min	20 min	30 min	40 min	Average
Estimated E_g	2.56 eV	2.35 eV	2.35 eV	2.35 eV	2.4 eV

The mean energy band gap value is $E_g = 2.4$ eV, lower than the expected value from literature (2.88 ÷ 3 eV) [47, 52].

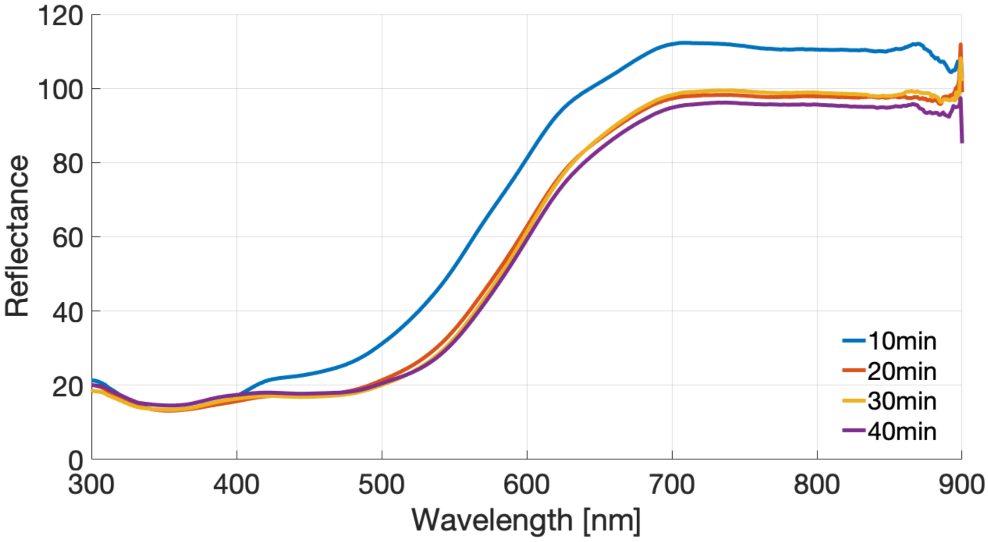

Figure 3.28: UV-Vis reflectance spectra of DMASnBr$_3$ pellets at different milling times.

3.2.2 In-Situ envrinomental tests

We again submitted some DMASnBr$_3$ powder to in-situ XRD measurements with the same methods discussed in 3.1. Figure 3.29 encodes all the relevant patterns (plus the reference pattern of DMASnBr$_3$ [2]) ascribed to environmental conditions (N_2, O_2, air, DI H_2O). As starting point we checked the pristine phase of DMASnBr$_3$ through diffraction under N_2 enviroment, figure 3.29(b) shows the first measured spectrum in inert conditions (N_2) compared with the crystallographic reference with excellent correspondence (Fig. 3.29(a)) , confirming the high structural quality of the synthesized material. The pristine sample has been then exposed to a continous O_2 flow in order to check the effect of oxygen on tin and therefore its possible oxidation. After 16 hours, the diffraction pattern remains unchanged (Figure 3.29(c)), confirming that oxygen alone does not significantly affect the crystalline framework of DMASnBr$_3$.

Upon exposure to ambient air (RH$\sim$ 60%) for 21 hours the sample undergoes partial degradation. As shown in Figure 3.29(d), the main reflections of DMASnBr$_3$ decrease in intensity while new peaks emerge; these new reflections can be assigned to Bis(dimethylammonium) Hexabromostannate compound, i.e. (DMA)$_2$SnBr$_6$ as confimred through comparison of new pattern with crystallogrpahic references (Figure 3.30), such transformation is clearly visible by looking at ■ refelctions superimposing in $10° < 2\Theta < 15°$. The partial convesion of DMASnBr$_3$ to (DMA)$_2$SnBr$_6$ indicates that tin is indeed oxydized from Sn^{2+} to Sn^{4+} and that oxygen alone is

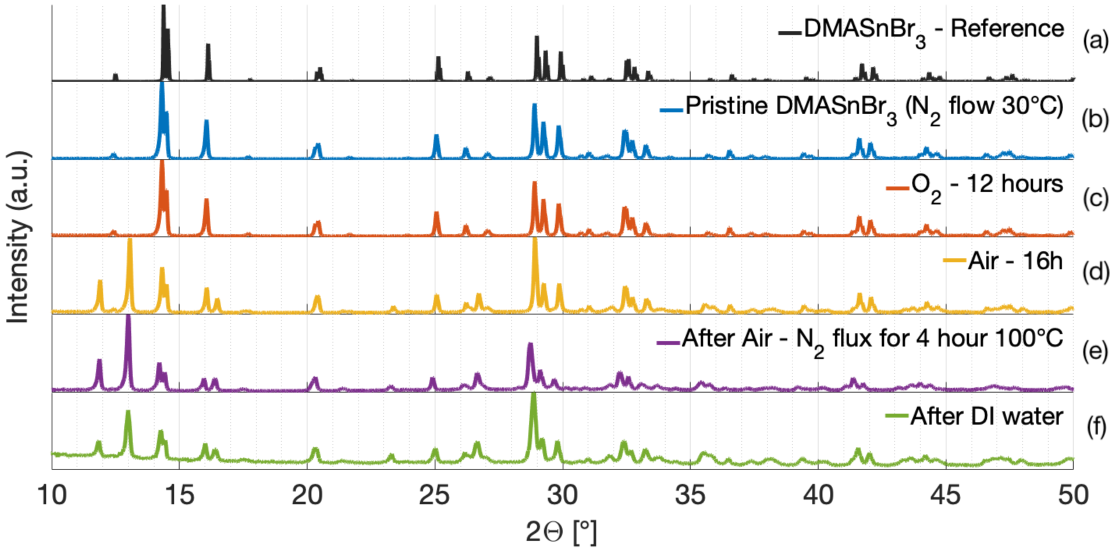

Figure 3.29: Overview of the most relevant in-situ XRD patterns of DMASnBr$_3$ with its crystallographic reference pattern (COD:96-810-3984 [2]).

not sufficient to drive such transformation, rather oxygen together with humidity promotes oxidation and relative structural rearrangement. Associated UV–Vis

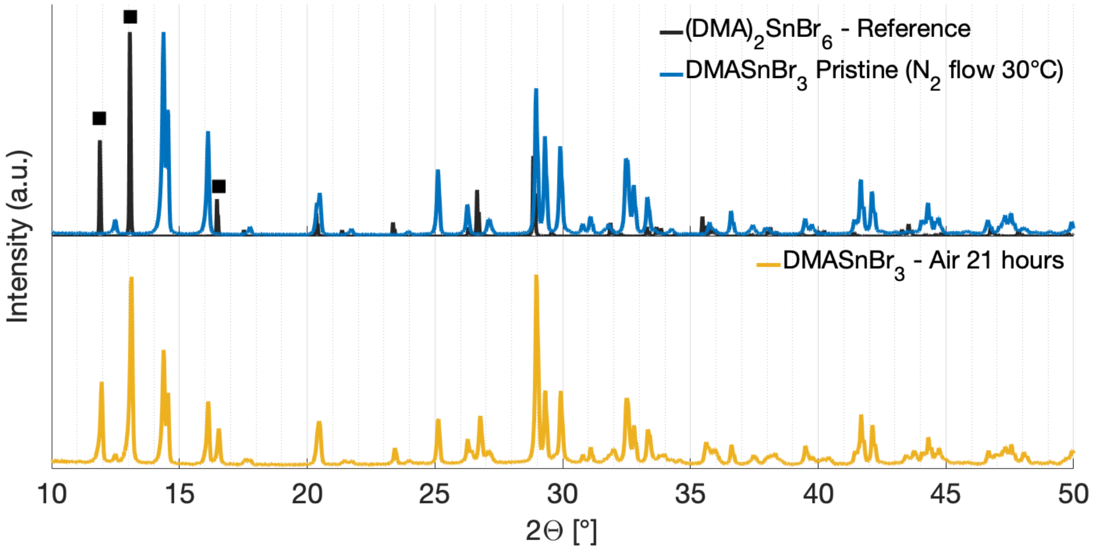

Figure 3.30: XRD pattern comparison of air exposed DMASnBr$_3$ with its pristine phase and crystallographic reference of (DMA)$_2$SnBr$_6$ (ICSD:110414 [7]).

measurements of air-exposed DMASnBr$_3$ show a redshift of the absorption edge for (Figure 3.31).

To test whether this optical redshift is caused by formation of the double perovskite, we synthesized ourselves (DMA)$_2$SnBr$_6$ by ball-milling DMABr and SnBr$_4$ and then measured both XRD (Fig. 3.32, that compared to literature reference assure us a correct synthesis) and its UVVis reflectance. Contrary to our hypothesis, experimentally synthesized (DMA)$_2$SnBr$_6$ exhibits a large blue-shift with respect to pristine and air exposed DMASnBr$_3$ samples (Fig. 3.31), therefore the redshift observed upon air exposure cannot be attributed solely to bulk conversion into (DMA)$_2$SnBr$_6$. However, the co-presence of (DMA)$_2$SnBr$_6$ and DMASnBr$_3$ might induce the formation of a heterojunction that, if wisely enginerred, might enhance photoelectro-conversion. Band gap values extrapolated from the reflectance spectra are written in table 3.4. Possible explanations for the discrepancy include formation of amorphous or highly disordered oxidised species (SnO$_2$), the emergence of sub-bandgap defect states associated with partial Sn oxidation (p-self doping), or the presence of absorbing surface residues that alter the effective reflectance. To identify the species (or combination of effects) responsible for the redshift, further characterisation is necessary (for example EDS/XPS to probe Sn oxidation state

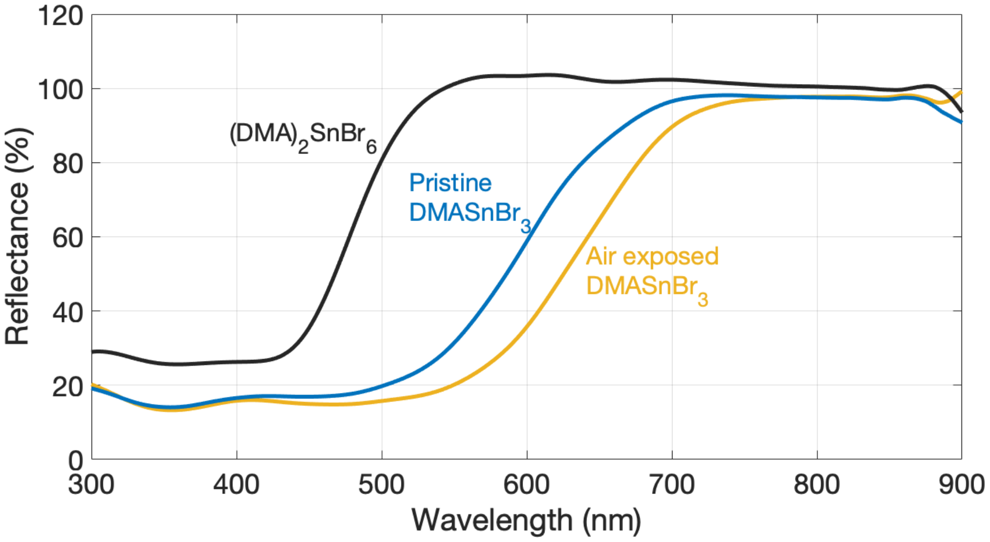

Figure 3.31: UVVis comparison of the new synthesized perovskite (DMA)$_2$SnBr$_6$ with pristine and air exposed DMASnBr$_3$.

Table 3.4: Band gap values estimated from the reflectance UVVis plots in figure 3.31. Pristine and Air samples refer to DMASnBr$_3$.

Sample	Pristine	Air	(DMA)$_2$SnBr$_6$
Estimated E_g	2.35 eV	2.14 eV	2.78 eV

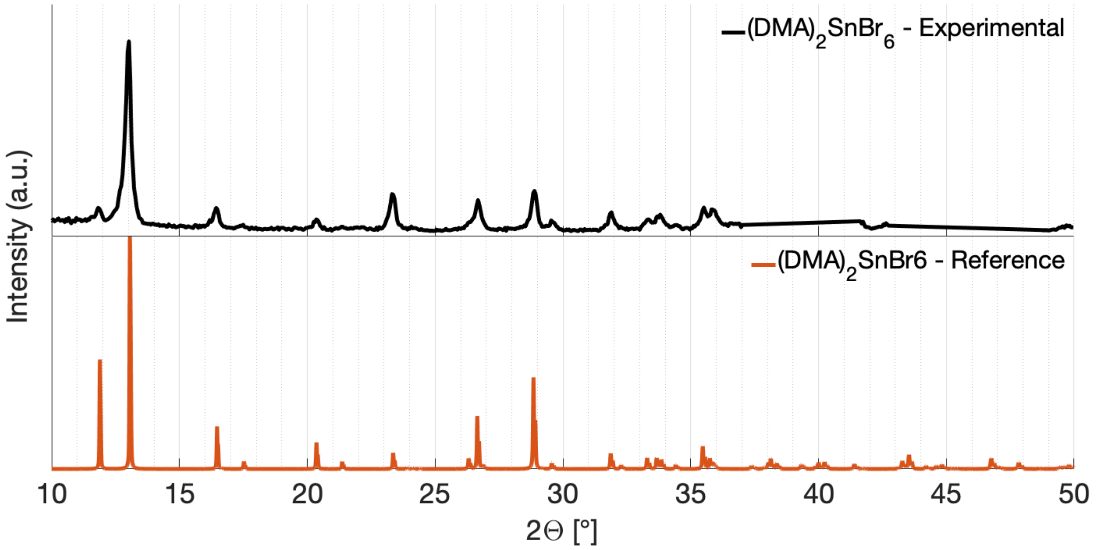

Figure 3.32: XRD pattern of experimentally synthesized $(DMA)_2SnBr_6$ with reference crystallographic pattern (ICSD:110414 [7]).

and elemental distribution, Raman/FTIR to detect new bonds, and photoluminescence or depth-resolved optical spectroscopy to probe sub-bandgap states).

Given the effect of air on $DMASnBr_3$, we tried to reverse such phase transformation, hence restoring the pristine phase, by subjecting the air exposed sample to N_2 atmosphere and heat in the attempt to degas oxygen and vapor from the powder. XRD patterns acquired after 1 hour at room temperature and after 4 hours at 100°C show unchanged patterns (Fig. 3.33), proving us that the heterojuction phase is stable and irreversible. Last but not least, the sample was subjected to a test in water. The air exposed sample has been wetted with DI water and subsequent XRD pattern was acquired. The latter revelad that the crystal phase associated to $DMASnBr_3$ - $(DMA)_2SnBr_6$ heterojunction (Fig. 3.34) is stable. The effect of water on this compound is only to decrease peaks' intensity, consistent with partial amorphization rather than the formation of a distinct hydrated phase. This behaviour is totally consistent with the one observed in literature by Romani et al. [49].

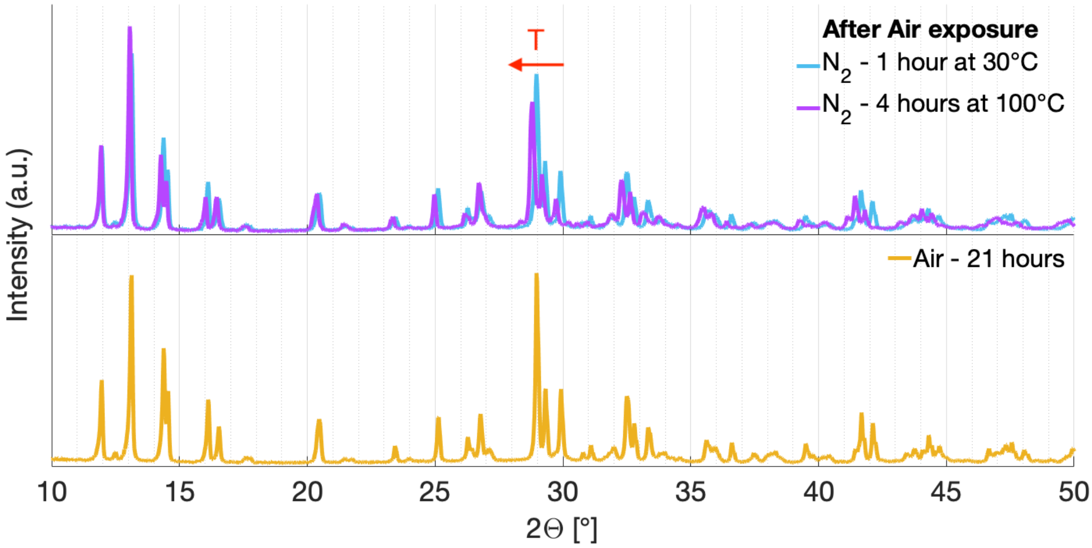

Figure 3.33: XRD pattern acquired duting the heat treatment in inert atmosphere (N$_2$) of DMASnBr$_3$ after air exposure. No significant changes happen upon heating, only a shift toward smaller 2Θ (due to lattice expansion) is noticeable in the 100°C spectrum with respect to the 30°C.

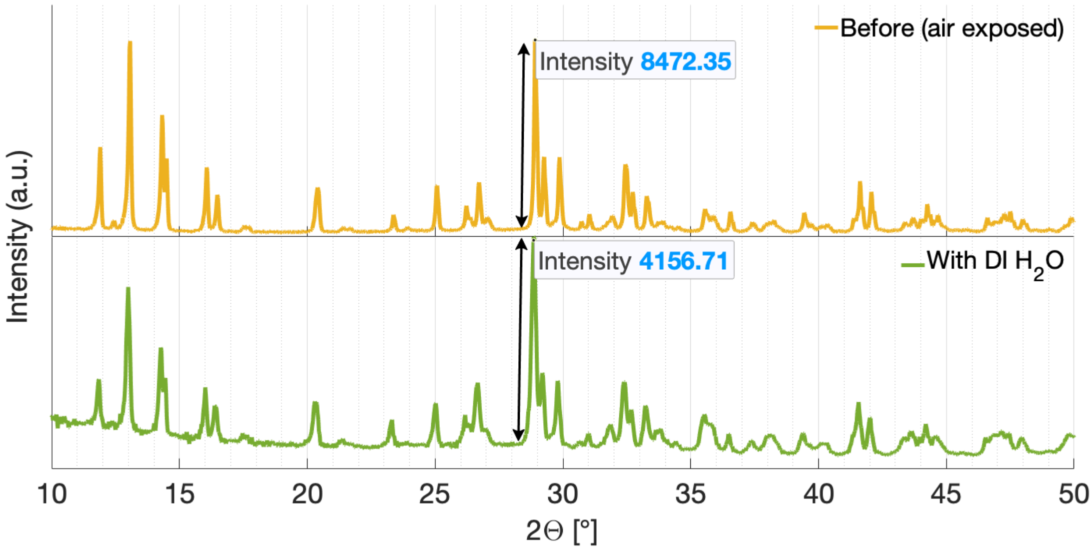

Figure 3.34: XRD pattern of air exposed DMASnBr$_3$ beofre and after contact with deionized water, compared with the 21 h air-exposed sample. Relative intensities of the main peak is showed to emphasize the effect of water.

Chapter 4

Conclusion

In this work we succesffuly proved the synthesis of two organic-inorganic tin-halide perovskites: dimethylammonium tin bromide ($DMASnBr_3$) and dymethilammonium tin iodide ($DMASnI_3$) powders with solvent-free ball-milling. Results from crystallographic diffraction patterns through XRD shown that both compounds completely form in the first 10-15 minutes of milling at 400 rpm.

Results from the in-situ XRD highlight the markedly different behaviour of $DMASnBr_3$ and $DMASnI_3$ when exposed to environmental agents.

$DMASnBr_3$ exhibits strong resistance to O_2, while it partially converts to vacancy ordered DMA_2SnBr_6 upon prolonged air exposure (21 hours), with moisture therefore acting as the main driving factor of such tranformation. Complementary UV-Vis analysis of the air exposed sample reveals a red shift in the reflectance spectrum with respect to pristine $DMASnBr_3$. However, reflectance spectrum of $(DMA)_2SnBr_6$ exhibits instead a blue shift relative to pristine $DMASnBr_3$. This incoherence suggest us that there're factors other than the crystalline phase of the material to count in. Co-existance of these two compounds may enhance phase stability upon contact with deionized water, given the excellent phase resilience observed in the diffraction pattern relative to water exposure.

In contrast, $DMASnI_3$ shows various phase instability. Oxygen alone is sufficient to both reduce crystallinity and to induce a visible color change from yellow to black, likely linked to amorphous conversion processes. Subsequent exposure to ambient air further accelerates the structural change, eventually leading to a new unkwon crystalline phases, which optically it retains the same black colour. An even more severe transformation was observed when in water by the appereance of SnI_4, confirming partial tin oxydation and turning to a yellow colour. Event tough we observed chromatic transformation upon air (from yellow to black) and in water (from black to yellow) we did not observed any phase reversibility as precedently stated in literature for this compound. By drying and heating the wetted powder under inert conditon (continous N_2 flow), it was not possible to restore the pristine phase, but rather when the powder completely dried from the water, it reveals a crystalline phase close to the air exposed one. TGA measurements instead, revelad that the air phase of $DMASnI_3$ has a lower onset temperature with respect to the pristine phase. $DMASnI_3$ thin films deposited through spin coating showed interesting high chromogenic sensibility to humid environment with reversible effect on the colour similar to powder.

Overall we asses the differecnes found in this work and the literature to be mostly attributed to the synthesis route of the two materials. As a matter of fact literature reports wet chemistry synthesized compound with micro-sized (or even bigger) crystals, whereas in our case, SEM pictures revelas that ball-milling can lead to nano-sized crystals, therefore what we observed as higher sensitivty and reactiviness within our materials can be explained by this difference.

Regarding possible solar aplications, $DMASnBr_3$ emerges as the more promising candidate among the two tin halide perovskites for photocatalytic applications and hydrogen evolution from water thanks to excellent phase stability, especially in water, and also thanks to its interesting "double-phase" when exposed to air, which in turn it might help to tune the band gap. On the other hand, $DMASnI_3$ suffers from irreversible structural and optical conversion under realistic environmental conditions, most of all there is the degradation to SnI_4 in water which makes it not compatible as active photocatalyst in water.

Chapter 5

Future works

The results presented in this thesis have demonstrated the feasibility of synthesizing lead-free pseudo-perovskites $DMASnBr_3$ and $DMASnI_3$ through a solvent free mechanochemical approach, and have provided new insights into their environmental stability. However, several aspects remain open for further investigation and could significantly advance the understanding and applicability of these materials. Possible future works on these compounds, and more generally about new THPs, should aim to complement their characterization. To make some examples: X-ray photon spectroscopy (XPS) measurements within the same set of environmental conditions can be implemented in order to get more precise and rigorous information about the elemental oxidation states, specifically regarding tin. Energy dispersive spectroscopy (EDS), coupled with SEM images, would be helpfull too in order to gather a chemical map of the compound within a range of environmental conditions. Also, exploiting UV-Vis instruments that can scan longer wavelenght can help us to estimate the actual band gap edge in $DMASnI_3$ "black" phase. Other characterization may be photoluminescence to gather information of charge transport through recombination rates. Moreover, by trying other synthesis paramters it would be possible to achieve different crystals size, hence allowing for tuning of the environmental sensitivity and reactivity to certain chemical species. Talking about thin films instead, in this work we reported a simple depostion method exploiting a solution composed of perovskite powder and 1-butanol as solvent. In this framework, future work can try new solvents, always following the green-chemistry guidelines, and how they might affect perovskite chemistry or structure during the depostion process. Otherwise, new routes and processes feasable with large scale-up, reproducibility and low environmental impact can be investigated as well. Regarding instead the compound synthesis, varying the paramteres set, i.e. ball-to-powder ratio, milling speed and time, could lead to an optimization of structure stability and photoconversion efficiency.

Bibliography

[1] National Renewable Energy Laboratory (NREL). Best research-cell efficiency chart. `https://www.nrel.gov/pv/cell-efficiency.html`, 2024. Accessed: 2024-05-20.

[2] G. Thiele and B. R. Serr. Crystal structure of dimethylammonium tribromostannate(II), (CH3)2nh2snbr3. *Zeitschrift für Kristallographie - Crystalline Materials*, 211(1):47, 1996.

[3] Crystal structure of dimethylammonium triiodostannate(ii), (ch3)2nh2sni3. *Zeitschrift für Kristallographie - Crystalline Materials*, 211(1):48–48, 1996.

[4] Linjuan Li, Dawei Xu, Xiankui Xu, Zheng Tian, Xue Zhou, Shenbo Yang, and Zhonghai Zhang. Modulation of active center distance of hybrid perovskite for boosting photocatalytic reduction of carbon dioxide to ethylene. *Proceedings of the National Academy of Sciences*, 121(7):e2318970121, 2024.

[5] Roscoe G. Dickinson. The crystal structure of tin tetra-iodide. *Journal of the American Chemical Society*, 45(4):958–962, 1923.

[6] I. Abrahams and D.Z. Demetriou. Inert pair effects in tin and lead dihalides: Crystal structure of tin(ii) bromide. *Journal of Solid State Chemistry*, 149(1):28–32, 2000.

[7] Keith B. Dillon, Joan Halfpenny, and Andrew Marshall. A variable-temperature 79br nuclear quadrupole resonance and x-ray crystallographic investigation of dimethylammonium hexabromostannate(iv), [nh2me2]2[snbr6]. *J. Chem. Soc., Dalton Trans.*, pages 1091–1094, 1983.

[8] R. D. Shannon. Revised effective ionic radii and systematic studies of interatomic distances in halides and chalcogenides. *Acta Crystallographica Section A*, 32(5):751–767, 1976.

[9] Ashley Marshall, Harry Sansom, Melissa McCarthy, Jonathan Warby, Olivia Ashton, Bernard Wenger, and Henry Snaith. Dimethylammonium: An A-site cation for modifying CsPbI3. *Solar RRL*, 5(11):2000599, 2020.

[10] International Energy Agency. Electricity 2025: Analysis and forecast to 2026, 2025. Accessed: [Insert Date].

[11] IPCC. Climate change 2022: Mitigation of climate change. working group iii contribution to the sixth assessment report of the intergovernmental panel on climate change, 2022.

[12] Michael G. Walter, Emily L. Warren, James R. McKone, Shannon W. Boettcher, Qixi Mi, Elizabeth A. Santori, and Nathan S. Lewis. Solar water splitting cells. *Chemical Reviews*, 110(11):6446–6473, 2010.

[13] Nathan S. Lewis. Research opportunities to advance solar energy utilization. *Science*, 351(6271):aad1920, 2016.

[14] Robert E. Blankenship, David M. Tiede, James Barber, Gary W. Brudvig, Graham Fleming, Maria Ghirardi, M. R. Gunner, Wolfgang Junge, David M. Kramer, Anastasios Melis, Thomas A. Moore, Christopher C. Moser, Daniel G. Nocera, Arthur J. Nozik, Donald R. Ort, William W. Parson, Roger C. Prince, and Richard T. Sayre. Comparing photosynthetic and photovoltaic efficiencies and recognizing the potential for improvement. *Science*, 332(6031):805–809, 2011.

[15] S. M. Sze and Kwok K. Ng. *Physics of Semiconductor Devices*. John Wiley & Sons, Hoboken, N.J., 3rd edition, 2007.

[16] Peng Yu and Guozhong Cao. Fundamental properties of semiconductor materials for solar energy conversion. In *Handbook of Photovoltaic Science and Engineering*, pages 87–148. John Wiley & Sons, Ltd, 2018.

[17] Frank E. Osterloh. Inorganic nanostructures for photoelectrochemical and photocatalytic water splitting. *Chemical Society Reviews*, 42(6):2294–2320, 2013.

[18] Hao Huang, Jie Yin, Weijie Ji, Yuxin Zhang, Xiaolin Li, Laiquan Li, Chao Ma, Dong Su, Zhongwei Chen, Chengjun Sun, Jun Luo, Shuangyin Wang, and Zhenxing Feng. Perovskite oxide based electrodes for efficient oxygen reduction and evolution reactions. *The Journal of Physical Chemistry C*, 123(13):17319–17327, 2019.

[19] Akihiko Kudo and Yugo Miseki. Heterogeneous photocatalyst materials for water splitting. *Chemical Society Reviews*, 38(1):253–278, 2009.

[20] Martin A. Green, Ewan D. Dunlop, Jochen Hohl-Ebinger, Masahiro Yoshita, Nikos Kopidakis, and Xiaojing Hao. Solar cell efficiency tables (version 62). *Progress in Photovoltaics: Research and Applications*, 31(7):651–663, 2023.

[21] Albert Polman, Mark Knight, Erik C. Garnett, Bruno Ehrler, and Wim C. Sinke. Photovoltaic materials: Present efficiencies and future challenges. *Science*, 352(6283):aad4424, 2016.

[22] Henry J. Snaith. Perovskites: The emergence of a new era for low-cost, high-efficiency solar cells. *The Journal of Physical Chemistry Letters*, 4(21):3623–3630, 2013.

[23] American Chemical Society. Perovskite, 2013. Accessed: June 3, 2024.

[24] D. B. Mitzi. Synthesis, structure, and properties of organic-inorganic perovskites and related materials. *Progress in Inorganic Chemistry*, 48:1–121, 2001.

[25] Bayrammurad Saparov and David B. Mitzi. Organic–inorganic perovskites: Structural versatility for functional materials design. *Chemical Reviews*,

116(7):4558–4596, 2016.

[26] Martin Green, Anita Ho-Baillie, and Henry Snaith. The emergence of perovskite solar cells. *Nature Photonics*, 8:506–514, 2014.

[27] Nam-Gyu Park and Hiroyuki Segawa, editors. *Multifunctional Organic–Inorganic Halide Perovskite: Applications in Solar Cells, Light-Emitting Diodes, and Resistive Memory.* Jenny Stanford Publishing, 1st edition, 2022.

[28] Jun Hong Noh, Sang Hyuk Im, Jin Hyuck Heo, Tarak N. Mandal, and Sang Il Seok. Chemical management for colorful, efficient, and stable inorganic-organic hybrid nanostructured solar cells. *Nano Letters*, 13(4):1764–1769, 2013.

[29] Stefaan De Wolf, Jakub Holovsky, Soo-Jin Moon, Philipp Löper, Bjoern Niesen, Martin Ledinsky, Franz-Josef Haug, Jun-Ho Yum, and Christophe Ballif. Organometallic halide perovskites: Sharp optical absorption edge and its relation to photovoltaic performance. *The Journal of Physical Chemistry Letters*, 5(6):1035–1039, 2014.

[30] Samuel D. Stranks, Giles E. Eperon, Giulia Grancini, Christopher Menelaou, Marcelo J. P. Alcocer, Tomas Leijtens, Laura M. Herz, Annamaria Petrozza, and Henry J. Snaith. Electron-hole diffusion lengths exceeding 1 micrometer in an organometal trihalide perovskite absorber. *Science*, 342(6156):341–344, 2013.

[31] Dominik Weber. Ch3nh3pbx3, ein pb(ii)-system mit kubischer perowskitstruktur / ch3nh3pbx3, a pb(ii)-system with cubic perovskite structure. *Zeitschrift für Naturforschung B*, 33(12):1443–1445, 2014.

[32] H. Huang, L. Polavarapu, J. A. Sichert, A. S. Susha, A. S. Urban, and A. L. Rogach. Colloidal lead halide perovskite nanocrystals: synthesis, optical properties and applications. *NPG Asia Materials*, 8(11):e328, 2017.

[33] Abdullah Y. Alsalloum, Bekir Turedi, Xiaopeng Zheng, Somak Mitra, Ayan A. Zhumekenov, Kwang Jae Lee, Partha Maity, Issam Gereige, Ahmed AlSaggaf, Iman S. Roqan, Omar F. Mohammed, and Osman M. Bakr. Low-temperature crystallization enables 21.9% efficient single-crystal MAPbI3 inverted perovskite solar cells. *ACS Energy Letters*, 5(2):657–662, 2020.

[34] Taame Abraha Berhe, Wei-Nien Su, Chen-Hao Chen, Ching-Jhih Chen, Meng-Che Tsai, Liang-Yih Chen, Amare Aregahegn Dubale, and Bing-Joe Hwang. Organometal halide perovskite solar cells: degradation and stability. *Energy & Environmental Science*, 9(2):323–356, 2016.

[35] Aslihan Babayigit, Anitha Ethirajan, Marc Muller, and Bert Conings. Toxicity of organometal halide perovskite solar cells. *Nature Materials*, 15(3):247–251, 2016.

[36] Michael Saliba, Taisuke Matsui, Ji-Youn Seo, Konrad Domanski, Juan-Pablo

Correa-Baena, Mohammad Khaja Nazeeruddin, Shaik M. Zakeeruddin, Wolfgang Tress, Antonio Abate, Anders Hagfeldt, and Michael Grätzel. Cesium-containing triple cation perovskite solar cells: improved stability, reproducibility and high efficiency. *Energy Environ. Sci.*, 9:1989–1997, 2016.

[37] Kohji Nishimura, Muhammad Akmal Kamarudin, Daisuke Hirotani, Kengo Hamada, Qing Shen, Satoshi Iikubo, Takashi Minemoto, Kenji Yoshino, and Shuzi Hayase. Lead-free tin-halide perovskite solar cells with 13 *Nano Energy*, 74:104858, 2020.

[38] George Volonakis, Amir Abbas Haghighirad, Rebecca L. Milot, WH Sio, Marina R. Filip, Bernard Wenger, Michael B. Johnston, Laura M. Herz, Henry J. Snaith, and Feliciano Giustino. Cs2inagcl6: A new lead-free halide double perovskite with direct band gap. *The Journal of Physical Chemistry Letters*, 8(4):772–778, 2017.

[39] Adam H. Slavney, Te Hu, Aaron M. Lindenberg, and Hemamala I. Karunadasa. A bismuth-halide double perovskite with long carrier recombination lifetime for photovoltaic applications. *Journal of the American Chemical Society*, 138(7):2138–2141, 2016.

[40] Malin B. Johansson, Huimin Zhu, and Erik M. J. Johansson. Crystal and electronic structures of complex bismuth iodides a3bi2i9 (a = k, rb, cs) related to perovskite: Aiding the rational design of photovoltaics. *J. Phys. Chem. C*, 123(3):1700–1708, 2019.

[41] D. B. Mitzi. Synthesis, structure, and properties of organic-inorganic perovskites and related materials. *Progress in Inorganic Chemistry*, 48:1–121, 1999.

[42] G. Grancini, C. Roldán-Carmona, I. Zimmermann, E. Mosconi, X. Lee, D. Martineau, S. Narbey, F. Oswald, F. De Angelis, M. Graetzel, and M. K. Nazeeruddin. One-year stable perovskite solar cells by 2d/3d interface engineering. *Nat. Commun.*, 8(1):15684, 2017.

[43] Samuel D. Stranks and Henry J. Snaith. Metal-halide perovskites for photovoltaic and light-emitting devices. *Nature Nanotechnology*, 10(5):391–402, 2015.

[44] Yangyang Dang, Yian Zhou, Xiaolong Liu, Dianxing Ju, Shengqing Xia, Haibing Xia, and Xutang Tao. Formation of hybrid perovskite tin iodide single crystals by top-seeded solution growth. *Angewandte Chemie International Edition*, 55(10):3447–3450, 2016.

[45] Shuyan Shao, Jian Liu, Hong-Hua Fang, Li Qiu, Gert H. ten Brink, Jan C. Hummelen, L. Jan Anton Koster, and Maria Antonietta Loi. Efficient perovskite solar cells over a broad temperature window: The role of the charge carrier extraction. *Advanced Energy Materials*, 7(22):1701305, 2017.

[46] Nakita K. Noel, Samuel D. Stranks, Antonio Abate, Christian Wehrenfennig, Simone Guarnera, Amir-Abbas Haghighirad, Aditya Sadhanala, Giles E. Eperon, Sandeep K. Pathak, Michael B. Johnston, Annamaria Petrozza,

Laura M. Herz, and Henry J. Snaith. Lead-free organic–inorganic tin halide perovskites for photovoltaic applications. *Energy & Environmental Science*, 7(9):3061–3068, 2014.

[47] Ambra Pisanu, Andrea Speltini, Paolo Quadrelli, Giovanni Drera, Luigi Sangaletti, and Lorenzo Malavasi. Enhanced air-stability of Sn-based hybrid perovskites induced by dimethylammonium (DMA): synthesis, characterization, aging and hydrogen photogeneration of the $\mathrm{MA}_{1-x}\mathrm{DMA}_x\mathrm{SnBr3}$ system. *Journal of Materials Chemistry C*, 7(23):7020–7026, 2019.

[48] Damiano Ricciarelli, Daniele Meggiolaro, Francesco Ambrosio, and Filippo De Angelis. Instability of tin iodide perovskites: Bulk p-doping versus surface tin oxidation. *ACS Energy Letters*, 5(9):2787–2795, 2020.

[49] Lidia Romani, Andrea Speltini, Francesco Ambrosio, Edoardo Mosconi, Antonella Profumo, Marcello Marelli, Serena Margadonna, Antonella Milella, Francesco Fracassi, Andrea Listorti, Filippo De Angelis, and Lorenzo Malavasi. Water-stable DMASnBr3 lead-free perovskite for effective solar-driven photocatalysis. *Angewandte Chemie International Edition*, 60(7):3611–3618, 2021.

[50] Naozumi Tanaka, Yoshitaka Kumabe, and Takashi Tachikawa. Impact of solvent-induced surface restructuring on charge carrier dynamics in DMASnI3. *ACS Applied Materials & Interfaces*, 17(24):35552–35561, 2025.

[51] Dianxing Ju, Xiaopeng Zheng, Jialiang Liu, Yan Chen, Jian Zhang, Bingqiang Cao, Hang Xiao, Omar F. Mohammed, Osman M. Bakr, and Xutang Tao. Reversible band gap narrowing of Sn-based hybrid perovskite single crystal with excellent phase stability. *Angewandte Chemie International Edition*, 57(45):14868–14872, 2018.

[52] Dianxing Ju, Gang Lin, Hang Xiao, Yuanyuan Zhang, Shigang Su, and Jian Liu. Investigation of water-stable perovskite $\mathrm{DMASnI}_x\mathrm{Br}_{3-x}$ for photoenzyme catalysis in aqueous solution. *Solar RRL*, 4(12):2000559, 2020.

[53] Constantinos C. Stoumpos, Christos D. Malliakas, and Mercouri G. Kanatzidis. Semiconducting tin and lead iodide perovskites with organic cations: Phase transitions, high mobilities, and near-infrared photoluminescent properties. *Inorg. Chem.*, 52(15):9019–9038, 2013.

[54] Wei-Qiang Liao, Dewei Zhao, Yue Yu, Corey R. Grice, Changlei Wang, Alexander J. Cimaroli, Philip Schulz, Weiwei Meng, Kai Zhu, Ren-Gen Xiong, and Yanfa Yan. Controlled crystallization of organic–inorganic hybrid perovskite films with superior optoelectronic performance via solid–liquid secondary growth. *J. Mater. Chem. A*, 4:16588–16595, 2016.

[55] Ayush Agrawal, Tavleen Singh, Sanjay K. Swami, Titas Dutta, and Rajiv K. Singh. Green solvent-based processing of perovskite solar cells. *ACS Sustain. Chem. Eng.*, 11(25):9285–9305, 2023.

[56] Daniel Prochowicz, Mohammad Mahdi Tavakoli, Shaik M. Zakeeruddin, Michael Grätzel, and Janusz Lewiński. Mechanoperovskites for photovoltaic applications: Preparation, characterization, and device fabrication. *Accounts*

of Chemical Research, 50(6):1431–1440, 2017.

[57] Xiaogang Feng, Jiang Li, Hong Wang, Jiandong Lang, Qiang Zhang, Weidong Zhu, Chengbing Wang, Jing Ma, Chunming Xu, Xianran Xing, et al. Mechanochemistry for ammonia synthesis under mild conditions. *Nat. Nanotechnol.*, 17(3):270–276, 2022.

[58] Tomislav Friščić, Cristina Mottillo, and Hatem M. Titi. Mechanochemistry for synthesis. *Angew. Chem. Int. Ed.*, 59(3):1018–1029, 2020.

[59] Stuart L. James, Christopher J. Adams, Carsten Bolm, Dario Braga, Paul Collier, Tomislav Friščić, Fabrizia Grepioni, Kenneth D. M. Harris, Geoffrey Hyett, William Jones, Anke Krebs, James Mack, Lucia Maini, A. Guy Orpen, Ivan P. Parkin, William C. Shearouse, Jonathan W. Steed, and Daniel C. Waddell. Mechanochemistry. *Chem. Soc. Rev.*, 41:413–447, 2012.

[60] Nicolas Fantozzi, Jean-Noël Volle, Andrea Porcheddu, David Virieux, Felipe García, and Evelina Colacino. Green metrics in mechanochemistry. *Chemical Society Reviews*, 52(19):6680–6714, 2023.

[61] Tridip Chutia and Dhruba Jyoti Kalita. Rational design of mixed sn–ge based hybrid halide perovskites for optoelectronic applications: a first principles study. *RSC Adv.*, 12:25511–25519, 2022.